



1 **Dynamic changes of optical and chemical properties of tar**  
2 **ball aerosols by atmospheric photochemical aging**

3 Chunlin Li,<sup>†</sup> Quanfu He,<sup>†</sup> Julian Schade,<sup>‡</sup> Johannes Passig,<sup>‡</sup> Ralf Zimmermann,<sup>‡</sup> Alexander  
4 Laskin,<sup>§</sup> and Yinon Rudich<sup>†,\*</sup>

5 <sup>†</sup>Department of Earth and Planetary Sciences, Weizmann Institute of Science, Rehovot 76100, Israel

6 <sup>‡</sup>Joint Mass Spectrometry Centre, University of Rostock, Dr.-Lorenz-Weg 2, 18059 Rostock, Germany

7 <sup>‡</sup>Joint Mass Spectrometry Centre, Cooperation Group ‘Comprehensive Molecular Analytics’ (CMA), Helmholtz  
8 Zentrum München, Ingolstädter Landstrasse 1, 85764 Neuherberg, Germany

9 <sup>§</sup>Department of Chemistry, Purdue University, West Lafayette, Indiana 47907, United States

10

11 *Correspondence to:* Yinon Rudich ([yinon.rudich@weizmann.ac.il](mailto:yinon.rudich@weizmann.ac.il))



12 **Abstract.** Following wood pyrolysis, tar ball aerosols were generated from wood tar separated into polar and  
13 nonpolar phases. Chemical information of fresh tar balls was obtained from a high-resolution time-of-flight  
14 aerosol mass spectrometer (HiRes-ToF-AMS) and single-particle laser desorption/resonance enhanced  
15 multiphoton ionization mass spectrometry (SP-LD-REMPI-MS). Their refractive index between 365 and 425  
16 nm was retrieved using a broadband cavity enhanced spectroscopy. Dynamic changes of the optical and  
17 chemical properties for the nonpolar tar ball aerosols in NO<sub>x</sub>-dependent photochemical process were  
18 investigated in an oxidation flow reactor (OFR). Distinct differences in the chemical composition of the polar  
19 and nonpolar tar aerosols were identified. Nonpolar tar aerosols contain predominantly high-molecular weight  
20 unsubstituted and alkyl-substituted polycyclic aromatic hydrocarbons (PAHs), while polar tar aerosols consist of  
21 a high number of oxidized aromatic substances (e.g., methoxy-phenols, benzenediol) with higher O:C ratio and  
22 carbon oxidation state. Fresh tar aerosols have light absorption characteristics similar to atmospheric BrC with  
23 higher absorption efficiency towards the UV wavelengths. The average retrieved refractive index (RI) are  
24  $1.661+0.020i$  and  $1.635+0.003i$  for the nonpolar and polar tar aerosols, respectively, with absorption Ångström  
25 exponent (AAE) between 5.7 and 7.8 in the wavelength region 365–425 nm. The RI fits a volume mixing rule  
26 for internally mixed nonpolar/polar tar aerosols. The RI of the tar aerosols decreased with increasing wavelength  
27 under photochemical oxidation. Photolysis by UV light (254 nm), without strong oxidants in the system, slightly  
28 decreased the RI and increased the oxidation state of the tar balls. Oxidation under varying OH exposure levels  
29 and in the absence of NO<sub>x</sub> diminished the absorption (bleaching), and increased the O:C ratio. The  
30 photobleaching of tar ball aerosols via photochemically induced OH-oxidation is mainly attributed to  
31 decomposition of chromophoric aromatics, nitrogen-containing organics, and high-molecular weight  
32 components. Photolysis of nitrous oxide (N<sub>2</sub>O) was used to simulate NO<sub>x</sub>-dependent photochemical aging of tar  
33 balls in the OFR. Under high NO<sub>x</sub> conditions, photochemical aging lead to the formation of organic-nitrates,  
34 increased oxidation degree and increased light absorption for the tar ball aerosols. These observations suggest  
35 that secondary organic nitrate formation compensates the bleaching by photolysis and OH radical  
36 photooxidation to eventually regain some absorption of aged tar balls aerosols. The atmospheric implication and  
37 climate effects from tar balls upon various oxidation processes are briefly discussed.



## 38 **1 Introduction**

39 Organic aerosol (OA), which represent a ubiquitous and dominant burden of the tropospheric particulate  
40 pollutants, play important roles in atmospheric chemistry and balance of regional and global radiation (Jimenez  
41 et al., 2009; Kanakidou et al., 2005; Seinfeld and Pandis, 2016; Shrivastava et al., 2017). An indirect climate  
42 influence of OA relies on their interaction with water thus acting as cloud condensation nuclei (CCN) that may  
43 alter the hydrological cycle (cloud formation and perception) and modify Earth's albedo (Forster and Taylor,  
44 2006; IPCC, 2013; Seinfeld and Pandis, 2016). The direct climate effect of OA is through extinction of  
45 incoming solar radiation and outgoing longwave radiation. Of particular importance is the warming effect due to  
46 light-absorbing carbonaceous aerosol commonly termed as brown carbon (BrC) (Andreae and Gelencsér, 2006).  
47 BrC is an important yet poorly understood OA component due to its complex physical properties, undefined  
48 chemical composition, and also its dynamic evolution under atmospheric processes (Adler et al., 2010; Moise et  
49 al., 2015; Laskin et al. 2015). It has been estimated that BrC accounts for 10-40% of the total light absorption in  
50 the atmosphere and when deposited on snow pack (Bahadur et al., 2012; Park et al., 2010), and contributes to  
51 global forcing of 0.10-0.25 W m<sup>-2</sup>, with even higher values on regional scales (Feng et al., 2013).

52 The origin of BrC can be either primary (i.e., directly emitted) or secondary (i.e., generated by reactions of  
53 aromatic or carbonyl compounds in clouds or particles) (Laskin et al., 2015). On a global scale, biomass burning  
54 releases over two-thirds of primary BrC and also contributes substantially to overall secondary OA formation  
55 (Jacobson, 2014; Jo et al., 2016). Better understanding of the optical properties of biomass burning BrC aerosols  
56 is crucial for constraining its atmospheric and climatic implications and Earth's energy balance. Unlike black  
57 carbon that absorbs light strongly throughout the entire UV-visible range, different chromophores that may also  
58 be coupled via charge transfer complexes enable BrC absorption in a much more pronounced and complicated  
59 wavelength-dependence manner (Phillips and Smith, 2004; Reid et al., 2005; Lin et al., 2016, 2017).

60 Tar balls are a specific type of particles produced from wood combustion (especially from biomass  
61 smoldering burning) which are abundant in the troposphere (Pósfai et al., 2004; Hand et al., 2005; Chen et al.,  
62 2017). Tar ball particles have been collected and identified in many biomass burning plumes (Pósfai et al., 2004;  
63 Fu et al., 2012; Li et al., 2017). Microanalysis has found that tar balls are homogeneous spherical carbonaceous  
64 particles with sizes ranging from tens to hundreds of nanometers. These particles contribute a considerable  
65 fraction of the biomass burning BrC (Pósfai et al., 2004; Hand et al., 2005; Li et al., 2017). The estimated  
66 burden of tar balls on regional and global climatic forcing has been emphasized. Tar balls from different burning



67 conditions and bio-fuels coexist with many other types of particles (e.g., inorganic salts, soot, and other  
68 carbonaceous aerosols in form of internal or external mixing), and these smoke particles undergo rapid  
69 atmospheric processing once they are released from the fire (Pósfai et al., 2004; Hand et al., 2005; Li et al., 2015,  
70 2017). However, *in situ* determination of the optical properties of these particles has not been reported due to  
71 inherent difficulty in selective tar balls sampling out of complex particle ensembles typical of field burning  
72 emissions.

73 The complex refractive index ( $RI=n+ki$ ,  $n$  and  $k$  are real and imaginary parts, corresponding to scattering  
74 and absorption, respectively) is an intrinsic optical property of aerosols. Quantifying the RI of OA is highly  
75 needed for evaluating the related radiative forcing influence (Moise et al., 2015). Recently, several studies have  
76 investigated the optical properties of tar ball particles (Chakrabarty et al., 2010; Hoffer et al., 2016;  
77 Sedlacek et al., 2018). The optical measurements reported for tar balls or other biomass burning BrC, were  
78 discrete over several wavelengths that were constrained by instruments measuring particle light coefficients, or  
79 indirectly inferred from calculations based on their electron energy-loss spectra or from UV-Vis absorption of  
80 solutions containing dissolved tar balls (Alexander et al., 2008). Hand et al. (2005) measured light scattering  
81 coefficients of tar balls-dominated fire plumes using a nephelometer, and reconstructed the scattering  
82 coefficients with simplified organic carbon (OC) and elemental carbon (EC) data to get an average RI of  
83  $1.56+0.02i$  for tar balls at  $\lambda = 632$  nm. Chakrabarty et al. (2010) measured the RI of tar ball particles from  
84 smoldering biomass combustion at 405, 532, and 780 nm, they observed a clear wavelength-, biofuel-, and even  
85 burning condition-dependent RI. The light absorption by tar balls was similar to humic-like substance (HULIS)  
86 with an imaginary part (0.002–0.015) that increased exponentially towards the near UV wavelengths. Recently,  
87 Hoffer et al. (2016) generated tar ball particles from flameless wood pyrolysis in the laboratory. They reported a  
88 higher RI value of  $1.84+0.2i$  at 550 nm, which fell closer to RI of soot than to that of HULIS. Large  
89 discrepancies reside in these results and discrete RI values make it difficult to decipher the complicated  
90 wavelength-dependence character of tar balls optical properties, which finally constrains the assessment of its  
91 radiative forcing effect.

92 Freshly emitted smoke BrC contain chromophores with diverse chemical structures, polarity, and  
93 volatility (Lin et al., 2016, 2017). After emission into the atmosphere, smoke particles undergo dynamic changes  
94 as a result of dilution, coagulation, and chemical processing on scales of seconds to days, which eventually  
95 affect the physiochemical properties of BrC particles during its lifetime in the atmosphere (Reid et al., 2005; Li  
96 et al., 2015; Laskin et al., 2015). Sumlin et al. (2017) simulated atmospheric photooxidation of biomass burning



97 BrC, and reported that photooxidation diminishes their light absorption. Zhong and Jang (2014) investigated the  
98 influence of humidity and NO<sub>x</sub> presence in photochemical aging of biomass burning BrC. They found that  
99 sunlight faded the color of BrC, and humidity facilitated the decay of light absorption by BrC, while presence of  
100 NO<sub>x</sub> delays the fading. Overall, they concluded that light absorption by BrC is governed by chromophores  
101 formation and bleaching by sunlight in the atmosphere. Therefore, evaluating the climatic impacts of tar ball  
102 particles requires more extensive investigation of its optical properties, and understanding of the dynamic  
103 transformations of the optical properties during atmospheric aging.

104 In this study, we generated proxies for tar ball particles by flameless wood pyrolysis (Tóth et al., 2014; Hoffer  
105 et al., 2016). This method allows consistent and continuous generation of tar ball proxy aerosols for studying  
106 their properties and processes. The RI of the tar aerosols as a function of wavelength in the ultraviolet-short  
107 visible region (365–425nm, 0.5 nm resolution) was determined using a broadband cavity enhanced spectrometer  
108 (BBCES). A high resolution time of flight aerosol mass spectrometer (HiRes-TOF-AMS) and a single-particle  
109 mass spectrometer applying laser desorption/resonantly enhanced multiphoton ionization (SP-LD-REMPI-MS)  
110 were used for probing the chemical profile of tar ball aerosols under NO<sub>x</sub>-dependent multiple-day  
111 photochemical oxidation. Specifically, the dynamic changes of their optical properties in correlation with their  
112 chemical composition were investigated. The atmospheric implications and climate forcing due to atmospheric  
113 aging of tar aerosols and evolution of their optical properties were also explored.

## 114 **2 Experiment**

### 115 **2.1 Tar ball particle generation**

116 Following the formation mechanism in biomass burning process, polydisperse tar ball particles were generated  
117 from droplets of wood tar in the laboratory (Tóth et al., 2014; Hoffer et al., 2016). In this study, a similar  
118 procedure was applied for producing tar ball aerosols. In brief, commercial wood pellets (Hallingdal Trepellets,  
119 water content of 6.55 wt.%, size of 2~3 cm in length, 0.2-0.3 cm in diameter) were smashed, heated and  
120 dry-distilled in absence of air (25°C min<sup>-1</sup> increase to 530 °C from room temperature, and held for 20 min at  
121 530 °C) to produce liquid tar-water emulsions (~25 mL per hundred grams of used wood pellets). The emulsions  
122 were filtrated using 0.45 μm pore size filter to remove particulate matter or solid precipitation. After overnight  
123 static stabilization, the wood tar solution was phase-separated into water soluble and non-soluble oily phases at  
124 an initial 3:1 volume ratio. Herein, we will term these two fractions as ‘polar’ and ‘nonpolar’ phases,  
125 respectively. The phase-separated solution was further concentrated using a heating plate at 300 °C with N<sub>2</sub>



126 purge flow to prevent oxidation. A final 1:1 volume ratio of polar to nonpolar phase was obtained; then the  
127 concentrated solutions were sealed and stored in the dark under 2 °C for following experiments. With respect to  
128 their potential reactivity and instability, the distillation products were used within a few days.

129 For optical properties measurement experiments, tar aerosols were produced by atomizing solutions of  
130 diluted tar in methanol (Gradient grade for HPLC, purity > 99.99 wt.%, Merck) with high-purity N<sub>2</sub> as a carrier  
131 gas. As the chemical composition for ambient tar balls is still unidentified, tar ball aerosols in this study were  
132 generated from polar, nonpolar, and mixtures of two phase tar solutions at volume mixing ratio of 2:1, 1:1, and  
133 1:2, respectively. Charcoal and quartz heating tubes (150 °C, residence time ~0.7s for particles at a nitrogen flow  
134 of 1.0 LPM) were used after the atomizer to outgas the methanol from the gaseous and particulate phases. Mesh  
135 filters (TSI) downstream were used to filter out ultrafine (less than 100 nm) particles.

## 136 2.2 NO<sub>x</sub>-dependent OH oxidation of tar ball aerosols

137 Heterogeneous oxidation of tar aerosols was simulated using an oxidation flow Reactor (OFR), shown  
138 schematically in Figure 1. The OFR has been characterized (Kang et al., 2007; Peng et al., 2015, 2016) and the  
139 operational procedures have been described previously (He et al. 2018). Briefly, the OFR consists of a  
140 horizontal 13.3 L aluminum cylindrical chamber (46 cm long × 22 cm ID) operating in continuous flow mode.  
141 The chamber is equipped with two power controllable ozone-free mercury-lamps with peak emission at λ = 254  
142 nm (82-934-08, BHK Inc., CA, USA). The two UV lamps are surrounded by Pyrex sheath tubes that are  
143 continuously purged with N<sub>2</sub> to cool the lamps and remove outgassing compounds. OH radicals in the OFR are  
144 produced through photolysis of externally introduced O<sub>3</sub> under 254 nm illumination and the further reaction of  
145 singlet oxygen (O<sup>1</sup>D) with water vapor:



148 External O<sub>3</sub> was produced by irradiation of 0.2 LPM high purity O<sub>2</sub> using a mercury lamp (λ = 185nm,  
149 78-2046-07, BHK Inc., CA). The O<sub>3</sub> concentration downstream of the OFR was measured with an O<sub>3</sub> monitor  
150 (2B Technology). A Nafion membrane humidifier (Perma Pure LIC, NJ) was used to supply water vapor to the  
151 OFR. Tar ball aerosols carried by 1.0 LPM N<sub>2</sub> flow from the atomizer were introduced into OFR. The initial  
152 aerosol concentrations in the OFR were mediated by controlling the concentration of the tar solution in the  
153 atomizer until the concentration of 350 nm particles was above 100 cm<sup>-3</sup>, as shown in Figure S1 of tar ball  
154 aerosols size distribution (SI, supporting information). Therefore, a total flow of 5.5 LPM with 36~38% RH,



155 initial 27~28 ppm O<sub>3</sub>, and 200~250 µg m<sup>-3</sup> tar ball particles (assuming material density of 1.0 g cm<sup>-3</sup>) was  
156 maintained, with a corresponding plug flow residence time (RT) of 144s for aerosols in the OFR.

157 The extent of simulated daytime oxidation by OH exposure was varied by changing the UV light intensity.  
158 Here, OH exposures in the OFR were inferred by measuring the decay of added SO<sub>2</sub> (using Thermo SO<sub>2</sub>  
159 analyzer, model 43i) due to reaction with OH radicals at specific UV lamp intensity. A low concentration  
160 (~60ppb) of SO<sub>2</sub> was used to minimize its influence on the OH radical reactivity. Typical total OH exposures  
161 ranged from (8.7±2.3)×10<sup>10</sup> to (8.6±1.7)×10<sup>11</sup> molec cm<sup>-3</sup> s or 0.5~7 equivalent daytime atmospheric oxidation  
162 days (EAD) were maintained, taking typical ambient average OH concentration as 1.5×10<sup>6</sup> molec cm<sup>-3</sup> (Kang et  
163 al., 2007; Peng et al., 2015, 2016).

164 In addition to reactions with oxidants, organic aerosols may change its chemical and physical properties by  
165 photolysis (Epstein et al., 2014; Lee et al., 2014; Wong et al., 2014). Therefore, the influence of light irradiation  
166 during tar ball photochemical aging was assessed at the short exposure time in the OFR. Here, tar balls aging  
167 was repeated at the same conditions (e.g., RT, RH, N<sub>2</sub>/O<sub>2</sub> flow, tar balls concentration, UV lamp power) without  
168 O<sub>3</sub> supply in the OFR. The 254 nm photon flux at specific to maximal UV lamp power was calculated by fitting  
169 the OH exposure estimated from SO<sub>2</sub> decay and by the Aerodyne OFR Exposure Estimator (v3.1,  
170 <https://sites.google.com/site/pamwiki/hardware/estimation-equations>).

171 Under polluted conditions, nitrogen oxides (NO<sub>x</sub>) are often involved in the atmospheric transformations of  
172 organic aerosol and alter their physiochemical properties (Rollins et al., 2012; Ng et al., 2007; Lin et al., 2015).  
173 Therefore, NO<sub>x</sub> influence on tar ball aerosol aging was also investigated. Due to rapid conversion of NO<sub>x</sub>  
174 (NO+NO<sub>2</sub>) into nitric acid (HNO<sub>3</sub>) under high O<sub>3</sub> and OH concentrations, simple addition of NO<sub>x</sub> into OFR  
175 cannot sustain NO<sub>x</sub> levels that compete with HO<sub>2</sub> radicals in the reaction with organic proxy (ROO). NO<sub>x</sub>  
176 generated via N<sub>2</sub>O reaction with O<sup>1</sup>D has been modeled and tested to suit the characterization of NO<sub>x</sub>-dependent  
177 SOA formation pathways using OFR (Peng et al. 2017; Lambe et al., 2017). In this study, N<sub>2</sub>O (99.999%)  
178 addition of 0.5 vol.% and 2.0 vol.% were used during tar ball aerosol photochemical oxidation in the OFR, and  
179 equivalent OH exposure of about 4.0 EAD was maintained. NO<sub>x</sub> (NO and NO<sub>2</sub>) concentrations downstream of  
180 the OFR was measured using a NO/NO<sub>2</sub> analyzer (Ecotech, Serinus 40 NO<sub>x</sub>). Experimental parameters  
181 including initial O<sub>3</sub> and N<sub>2</sub>O concentrations, NO<sub>x</sub>, moisture ratio, maintained OH exposures and the  
182 corresponding photon flux at 254 nm are presented in Table 1.

### 183 2.3 Online optical and chemical characterization



184 Prior to the optical measurements, excess ozone and NO<sub>x</sub> were removed from the sample air stream following  
185 the OFR using two diffusion denuders packed with Carulite (Carus Corporation, Peru, IL) and one activated  
186 charcoal tube. The stream flow was further dehydrated with two silica gel diffusion dryers. Afterward, the tar  
187 ball aerosols were characterized by a combination of on-line chemical and optical instruments.

188 Bulk chemical fragments and organic elemental ratios of tar ball aerosols were monitored in real time by the  
189 HiRes-ToF-AMS (Aerodyne Research Inc., Billerica, MA, USA) in alternating high sensitivity V and  
190 high-resolution W modes. The working principles of the AMS have been described in details elsewhere  
191 (DeCarlo et al., 2006). In short, aerosol particles are separated from the gas phase through an aerodynamic lens  
192 system and then transferred into the vacuum system, where they are impacted onto a vaporizer at about 600 °C,  
193 thus vaporizing the particles. The analyte vapors are ionized with 70 eV electron impact ionization (EI). A  
194 time-of-flight mass spectrometer is used for high-resolution analysis of the ions. SQUIRREL v1.16 and PIKA  
195 v1.57 codes (<http://cires.colorado.edu/jimenez-group/ToFAMSResources/ToFSoftware/>) were used to process  
196 the collected AMS data. Four ion groups were classified as C<sub>x</sub>H<sub>y</sub><sup>+</sup>, C<sub>x</sub>H<sub>y</sub>O<sup>+</sup>, C<sub>x</sub>H<sub>y</sub>O<sub>z</sub><sup>+</sup> (z>1), and C<sub>x</sub>H<sub>y</sub>O<sub>i</sub>N<sub>p</sub><sup>+</sup> (i≥0,  
197 p≥1) based on fragment features. The ions O<sup>+</sup>, OH<sup>+</sup>, and H<sub>2</sub>O<sup>+</sup> were included in the C<sub>x</sub>H<sub>y</sub>O<sub>z</sub><sup>+</sup> group, as  
198 concentrations of these species were calculated from the organic CO<sub>2</sub><sup>+</sup> ion abundance using the method in Aiken  
199 et al (2008). The ambient improved (AI) atomic ratios of oxygen to carbon (O:C), hydrogen to carbon (H:C),  
200 nitrogen to carbon (N:C), and organic mass to organic carbon (OM/OC) were generated from the measured ion  
201 fragments.

202 Particle-bound organic molecules were measured using a custom single-particle time-of-flight mass  
203 spectrometer. This instrument features laser desorption and resonantly enhanced multiphoton ionization  
204 (SP-LD-REMPI-ToF-MS), allowing for the detection of aromatic substances on individual particles. Detailed  
205 description and application of the instrument in LD-REMPI ionization mode is given by Bente et al. (2008) and  
206 Passig et al. (2017). Briefly, aerodynamically accelerated particles are individually sized using laser velocimetry,  
207 and heated by a pulsed CO<sub>2</sub> infrared laser (10.6 μm) to desorb organic molecules. Aromatic substances in the  
208 gas plume are selectively ionized via REMPI by a KrF-excimer laser pulse (248 nm) and detected in the positive  
209 MS flight tube. The REMPI-MS technique is very sensitive and selective for aromatic substances (Boesl et al.,  
210 1978; Grottemeyer et al., 1986; Rettner and Brophy, 1981) and suitable for studies on pyrolysis and (wood)  
211 combustion processes (Heger et al., 1999; Czech et al., 2017). For the tar ball aerosols it provides  
212 complementary information to the HiRes-TOF-AMS spectra. A custom software on LabView basis records and  
213 calculates the aerodynamic size and individual mass spectra of the particles.





214 For optical measurements, tar ball aerosols were size-selected using an Aerosol Aerodynamic Classifier (AAC,  
215 Cambustion, UK). AAC has significant advantages over the commonly used Differential Mobility Analyzer  
216 (DMA) classifier. The AAC classifies particles based on the aerodynamic size without charging and hence it  
217 avoids the contribution of multiply charged particles, thus generating real monodisperse size-selected particles  
218 distribution, reducing the errors associated with multiply charged large particles. In addition, the AAC has  
219 higher particle transmission efficiency at the relevant size range (Tavakoli and Olfert, 2013, 2014).  
220 Aerodynamic size-classified particles after the AAC were further scanned by a scanning mobility particle sizer  
221 (SMPS, classifier Model 3080, DMA Model 3081, CPC model 3775, TSI) to derive their mobility size  
222 distribution. The effective density of the tar balls was estimated assuming a shape factor of particle to be 1.0  
223 (sphericity was verified using a scanning electron microscopy in this study):

$$224 \rho_{eff} = \frac{D_{aero}}{D_m} \rho_0 \quad [1]$$

225 Where  $\rho_{eff}$  is an effective density,  $D_{aero}$  and  $D_m$  are aerodynamic and mobility diameters, respectively.  $\rho_0$  is unit  
226 density of 1.0 g cm<sup>-3</sup>.

227 Based on the derived effective density, size-specific tar aerosols covering mobility diameters between 175 to  
228 350 nm with an interval of 25 nm were size-selected via AAC and introduced into a dual-channel broad-band  
229 cavity enhanced spectrometer (BBCES) for light extinction ( $\alpha_{ext}$ ) measurements in the wavelength of 360~395  
230 nm and 385~435 nm (at resolution 0.5 nm). A detailed description of the instrument can be found elsewhere  
231 (Washenfelder et al., 2013; Flores et al., 2014a, b). With the combination of a condensation particle counter (TSI  
232 3575) to measure particle concentration ( $N$ ) in series, size-specific particle extinction cross section ( $\sigma_{ext}$ ) can be  
233 calculated by Equation (2):

$$234 \sigma_{ext}(\lambda, D_p, RI) = \frac{\alpha_{ext}(\lambda, D_p, RI)}{N(D_p)} \quad [2]$$

235 Where  $\lambda$  is the wavelength of incidence light,  $D_p$  is the particle mobility diameter.

236 Using the Mie-Lorenz scattering theory, the wavelength-dependent complex refractive index of spherical  
237 homogeneous particles was derived (Pettersson et al. 2004; Abo Riziq et al. 2007). The retrieval algorithm was  
238 limited to search for  $n \geq 1$  and  $k \geq 0$  as their physical boundaries. Thereafter, spectral dependent extinction,  
239 scattering, and absorption cross sections ( $\sigma_{ext}$ ,  $\sigma_{sca}$ , and  $\sigma_{abs}$ ) were calculated from the complex RI at specific  
240 particle size. Using these parameters, the single scattering albedo, indicating the scattering fraction of light  
241 extinction ( $SSA = \sigma_{sca}/\sigma_{ext}$ ), was calculated.

242 The absorption and extinction Ångström exponents ( $\hat{A}_{abs}$  and  $\hat{A}_{ext}$ ) describe the spectral dependence of aerosol



243 light properties, and are widely used in climate modeling (Russell et al., 2010). It is customary to extrapolate the  
 244 optical spectral absorption and extinction fitting to the range of wavelengths using a power law  $\propto \lambda^{-A_{abs}}$  and  
 245  $\propto \lambda^{-A_{ext}}$ , respectively. In this work, we determined  $\hat{A}_{ext}$  and  $\hat{A}_{abs}$  with a linear regression of  $\ln(\sigma_{ext})$  and  $\ln(\sigma_{abs})$   
 246 against  $\ln(\lambda)$  over the range of 365 to 425 nm:

$$247 \quad \hat{A}_{ext} = -\frac{\ln(\sigma_{ext})}{\ln(\lambda)} \quad \hat{A}_{abs} = -\frac{\ln(\sigma_{abs})}{\ln(\lambda)} \quad [3]$$

248 Here  $\hat{A}_{ext}$ ,  $\hat{A}_{abs}$ , and SSA were calculated for tar ball aerosols with a median diameter of 150 nm.

#### 249 **2.4 Offline optical characterization**

250 In addition to the *in-situ* measurements, tar ball particles were also collected quantitatively onto Teflon filters  
 251 (47 mm diameter, 0.45  $\mu\text{m}$  porosity, Pall Corp.) at sampling flow rate of 2 LPM and then extracted using  
 252 methanol (HPLC grade, Merck) for offline UV-Vis absorption measurement (Cary 60 UV-VIS spectroscopy,  
 253 Agilent). Methanol extraction of organic compounds has been commonly performed in various studies (Hoffer  
 254 et al., 2006; Laskin et al., 2009; Yee et al., 2013; Finewax et al., 2018; Xie et al., 2017). Here we verified the  
 255 completeness of the extraction by extracting each filter twice with methanol. Moreover, vortex shaking (Vortex  
 256 Genie-2, Scientific Industries) rather than sonication was applied to avoid chemical degradation of the extracts  
 257 upon ultrasonic irradiation (Miljevic et al., 2014; Mutzel et al., 2013). The mass absorption cross section (MAC,  
 258  $\text{m}^2 \text{g}^{-1}$ ) and refractive imaginary  $k$  of the dissolved tar ball materials were estimated based on following relations  
 259 (Chen and Bond, 2010):

$$260 \quad MAC_{(\lambda)} = \frac{Abs_{(\lambda)} \times \ln(10)}{C \times b} \quad [4]$$

$$261 \quad k_{(\lambda)} = \frac{\lambda \times \rho \times MAC_{(\lambda)}}{4\pi} \quad [5]$$

262  $Abs_{(\lambda)}$  is the base-10 absorbance result from UV-VIS spectroscopy (unitless),  $b$  is the optical length of the  
 263 solution,  $C$  is the mass concentration of solution ( $\text{g m}^{-3}$ ),  $\lambda$  is the incident light wavelength, and  $\rho$  is material  
 264 density ( $\text{g cm}^{-3}$ ). Here, the derived effective density  $\rho_{eff}$  was used. The absorption Ångström exponent based on  
 265 MAC was also derived as  $\hat{A}_{abs-UV-Vis}$  over the 365-425 nm spectral range.

266 In addition, particles were impacted at a flow of  $2.5 \text{ L min}^{-1}$  onto cyclopore track-etched polycarbonate  
 267 membrane (47 mm, 0.1  $\mu\text{m}$  porosity, Whatman Inc.) to investigate the morphology of tar balls using Scanning  
 268 Electronic Microscopy (SEM, JEOL JSM-7000F).

#### 269 **2.5 Radiative impacts of tar ball aerosols**



270 To assess the climatic influence of tar ball particles, a wavelength-dependent direct shortwave aerosol simple  
271 radiative forcing efficiency (SRF,  $\text{W g}^{-1}$ ) was estimated using the clear sky air mass global horizontal solar  
272 spectrum (AM1GH), assuming that tar ball aerosols form a uniform, optically thin aerosol layer at the lower  
273 troposphere or on ground (Bond and Bergstrom, 2006; Levinson et al., 2010):

$$274 \quad \frac{dSRF}{d\lambda} = -\frac{1}{4} \frac{dS(\lambda)}{d\lambda} \tau_{atm(\lambda)}^2 (1 - F_c) [2(1 - R_{sfc})^2 \beta_{(\lambda)} MSC_{(\lambda)} - 4R_{sfc} \cdot MAC_{(\lambda)}] \quad [6]$$

275 Where  $dS(\lambda)/d\lambda$  is the solar irradiance ( $\text{photons s}^{-1} \text{cm}^{-2}$ ),  $\tau_{atm}$  is the atmospheric transmission (taking 0.79 for  
276 simple calculation),  $F_c$  is the cloud fraction (approximately 0.6),  $R_{sfc}$  is the surface albedo (approximate 0.19 for  
277 urban area ground and 0.8 for snow) (Chen and Bond, 2010),  $\beta$  is the average up-scatter fraction (the fraction of  
278 scattered sunlight that is scattered into the upward hemisphere), and  $MSC(\lambda)$  is wavelength-dependent mass  
279 scattering cross section, respectively. We simply calculated radiative forcing of particles with atmospheric  
280 relevant size of 50 to 500 nm, and SRF was estimated and integrated over the measured range of 365~425nm.  
281 The actinic flux over 365~425 nm was obtained from the “Quick TUV Calculator”, available at  
282 [http://cprm.acom.ucar.edu/Models/TUV/Interactive\\_TUV/](http://cprm.acom.ucar.edu/Models/TUV/Interactive_TUV/) using the following parameters: SZA (solar zenith  
283 angle) of 0 degree, noon time, June 30, 2000, 300 Dobson overhead ozone column, surface albedo of 0.19 for  
284 urban area and 0.8 for snow, and 0 km altitude.

### 285 3 Results and discussion

#### 286 3.1 Chemical composition and optical properties of fresh tar ball aerosols

287 The chemical composition and optical properties of fresh tar ball aerosols generated from polar, nonpolar, and  
288 mixtures of the two-phase tar solutions were characterized. The bulk mass spectra for polar and nonpolar tar ball  
289 particles are shown in Figure 2. The mass spectra features and particle effective densities are summarized and  
290 compared in Table S1. Distinct differences in the chemical composition were observed between polar and  
291 nonpolar tar ball aerosols. The alkyl fragments ( $\text{C}_x\text{H}_y^+$ , e.g.,  $\text{C}_n\text{H}_{2n-1}^+$ ,  $\text{C}_n\text{H}_{2n+1}^+$ ) dominate the signals for  
292 nonpolar particles (accounting for ~56% of total fragments), implying that the nonpolar tar aerosols have  
293 compositional similarity with common hydrocarbon organic aerosol (HOA). The  $\text{C}_x\text{H}_y\text{O}^+$  fragments are the  
294 primary ions for the polar tar aerosols, contributing ~42% of their mass spectrum, suggesting that most of the  
295 organic constituents in the polar tar aerosols are substantially oxygenated. Both spectra exhibit significant  
296 intensity at  $m/z$  28 ( $\text{CO}^+$ ),  $m/z$  29 ( $\text{CHO}^+$ ), and  $m/z$  43 ( $\text{C}_2\text{H}_3\text{O}^+$ ), indicating the presence of carbonyl ions. The  
297 strong signal at  $m/z$  31 ( $\text{CH}_3\text{O}^+$ ) results from methoxy species that preferably partition into the polar tar fraction.



298 In addition, the significant signals at  $m/z$  50-52 ( $C_4H_2^+$ ,  $C_4H_3^+$ ,  $C_4H_4^+$ ),  $m/z$  65 ( $C_5H_5^+$ ),  $m/z$  77-78 ( $C_6H_5^+$ ,  $C_6H_6^+$ ),  
299  $m/z$  81 ( $C_6H_9^+$ ), and  $m/z$  91 ( $C_7H_7^+$ ), which are characteristic of aromatic compounds, indicate that tar aerosols,  
300 especially from the nonpolar phase, contain a considerable amount of aromatic organics or present high  
301 aromaticity. Ion peaks at  $m/z$  77-78, 81, and 91 are typical for monocyclic aromatics such as alkyl-substituted  
302 benzene (for  $m/z$  77-78, 91) and heterocyclic aromatics (for  $m/z$  81) (Li et al., 2012). While the relative higher  
303 signal at  $m/z$  128 ( $C_{10}H_8^+$ ) in the nonpolar tar aerosols mass spectra can be assigned to molecular ion of  
304 naphthalene (Herring et al., 2015). Moreover, signals at  $m/z$  55 and 57 ( $C_3H_3O^+$ ,  $C_3H_5O^+$ ) are signature  
305 fragments of aliphatic and non-acid oxygenated organics that are used to trace cooking emissions (He et al.,  
306 2010), and these two fragments were also observed in the tar ball aerosols. Similar to ambient biomass burning  
307 emissions,  $C_2H_4O_2^+$  ( $m/z$  60) and  $C_3H_5O_2^+$  ( $m/z$  73), two characteristic fragments from levoglucosan and similar  
308 cellulose pyrolyzed species (mannosan, galactosan) were detected in all the tar aerosols, and these fragments  
309 were more prominent in the polar aerosols due to the solubility of levoglucosan and analogs in water. Weimer et  
310 al. (2008) reported the percentage of  $m/z$  60 and 73 for the burning of various woods to be 0.6-4.1% and  
311 0.1-2.0%, respectively. The percentage of these two fragments in the tar aerosols (0.7-1.6% for  $m/z$  60 and  
312 0.5-0.9% for  $m/z$  73) are comparable to the literature data, although the fuel and the pyrolysis procedure are  
313 different. The  $m/z$  137 peak is dominated by fragments of  $C_8H_9O_2^+$  and  $C_7H_5O_3^+$ , and these fragments have been  
314 determined in biomass burning emissions and were assigned to lignin-related ions with methoxy-phenolic  
315 structures (Li et al., 2012; Li et al., 2014). Phenols and methoxy phenols are prominent compounds, accounting  
316 for 41% of the identified organic species, in primary BBOA (Schauer et al., 2001). The signal at  $m/z$  137 is  
317 much higher in the nonpolar phase aerosols (1.0% and 0.5% for nonpolar and polar tar balls, respectively), and  
318 the fraction of fragment  $m/z$  137 is consistent with reference values of 0.3-2.0% (Li et al., 2012).  $m/z$  44 ( $CO_2^+$ ),  
319 a marker fragment of carboxylic acids has been parameterized as  $f_{44}$  (fraction of mass spectrum signal at  $m/z$  44)  
320 to present the oxidation degree of organic aerosols (Aiken et al., 2008; Ng et al., 2010). Higher  $f_{44}$  values  
321 indicate more oxidized OA (OOA), while less oxidized OA is characterized by lower  $f_{44}$  (Schauer et al., 2001).  
322 Peroxides can also produce  $CO_2^+$  signal via extensive fragmentation in the AMS (Aiken et al., 2008).  $f_{44}$  has  
323 also been shown to be linearly correlated with the elemental O:C ratio of OA (Aiken et al., 2008). In this study,  
324  $f_{44}$  for the nonpolar and polar tar aerosols are 1.9% and 2.4%, and the corresponding O:C ratios are 0.25 and  
325 0.44. The higher O:C and H:C ratios explain the polarity of the polar tar ball aerosols. The simplified average  
326 carbon oxidation state ( $\overline{OSc} \approx 2O:C-H:C$ ) describe the oxidation level of particulate complex organic mixtures  
327 (Kroll et al., 2011). The calculated  $\overline{OSc}$  for the tar ball aerosols are -1.05~-0.76, which agrees well with reference



328 values of -1.0~-0.7 for primary BBOA (Kroll et al., 2011). These values are in the broad range of -1.7~-1.6 for  
329 HOA and -0.5~0 for semivolatile OOA (Aiken et al., 2008). In addition, a small fraction of nitrogen-containing  
330 organic compounds (NOC) was detected, with the  $C_xH_yO_iN_p^+$  group contributing 1.6~3.6% of the tar balls mass  
331 spectra with estimated N:C ratio below 0.01, which agrees with previously reported N:C values of 0.008~0.018  
332 for biomass burning emissions (He et al., 2010). Biomass burning is an important source of NOC in the  
333 atmosphere: alkaloid and nitro-aromatic constituents were detected to be abundant constituents of the NOC  
334 (Laskin et al., 2009; Lin et al., 2017). Nitroaromatic compounds were also identified in urban fire emissions  
335 (Bluvshstein et al., 2017; Lin et al., 2017). Although these compounds constitute a small fraction of the BBOA  
336 mass, these chromophoric NOC species accounted for 50~80% of the total visible light absorption by the  
337 extractable BrC (Lin et al., 2017).

338 Fragments larger than 100 amu ( $f_{m/z>100}$ ) contribute a large fraction of the total organic signals for tar ball  
339 aerosols, consistent with biomass burning emissions that contain a large fraction of high-molecular weight  
340 compounds (Ge et al., 2012; Zhou et al., 2017).  $f_{m/z>100}$  is 32% for the nonpolar tar ball aerosols, which is higher  
341 than that of the polar particles (15%), demonstrating that the nonpolar tar balls consists of more high-molecular  
342 weight organics. The measured effective densities for polar and nonpolar tar balls are 1.33 and 1.24 g cm<sup>-3</sup>.  
343 Chemical characteristics from AMS and densities for internal mixture tar balls follow the volume-linear mixing  
344 of polar and nonpolar tar solutions.

345 A considerable aromatic fraction in the tar ball aerosols was confirmed by the LD-REMPI-MS measurement.  
346 Figure 3 presents the mass spectra of aromatic substances obtained for each one exemplary polar and one  
347 nonpolar particle, respectively. Aerodynamic size distributions for the detected tar ball aerosols are given in  
348 Figure S2, and substances identified in the mass spectra are listed in Table S2. The features in the mass spectra  
349 are consistent with the polarity of examined tar ball aerosols. The complex REMPI-spectrum shows rows of  
350 intense unsubstituted and partially alkylated PAH peaks in the nonpolar tar balls, including naphthalene,  
351 acenaphthylene, phenanthrene, pyrene, and in particular, the softwood combustion marker retene at  $m/z$  234 and  
352 some possible derivatives (oxidized-retene at  $m/z$  250 with one oxygen addition, methyl-retene at  $m/z$  248 with  
353 one methyl addition) (McDonald et al., 2000; Shen et al., 2012). Retene and some of the aforementioned PAHs  
354 are also observed in the polar aerosols' mass spectra with lower intensities. In contrast, the polar tar ball REMPI  
355 mass spectrum shows strong peaks from oxidized aromatics, more specifically, benzenediol and  
356 methoxy-phenols (indicating e.g. catechol, guaiacol, acetovanillone, syringaldehyde, coniferyl aldehyde, etc.).  
357 These results correspond to the large fractions of  $CHO^+$  and  $CH_3O^+$  fragments and high O:C ratios observed for



358 the polar tar aerosols via HiRes-TOF-AMS, and are consistent with the strong signals of typical aromatic  
359 fragments observed in the nonpolar tar aerosols in Figure 2. The dominance of aromatic compounds in tar ball  
360 chemical composition agrees well with previous work on BBOA (Schauer et al., 2001; Wei et al., 2015; Bente et  
361 al. 2008, 2009; Czech et al. 2017). Biomass burning is a major source of environmental PAHs (alkylated PAHs,  
362 oxygenated-PAHs, phenols, nitrogen-substituted PAHs, etc.) in both particulate and gaseous phases, and  
363 extensive emissions of PAHs from incomplete combustion pose a great threat to ecosystem and human health  
364 due to their carcinogenic toxicity (Li et al., 2017; Shen et al., 2013; Sigsgaard et al., 2015; Shrivastava et al.,  
365 2017). Moreover, the primary PAHs can act as precursors that substantially contribute to ambient SOA or BrC  
366 when involved in atmospheric photochemical aging, leading to profound climatic influence (Yee et al., 2013; Yu  
367 et al., 2014; Lu et al., 2011; Zhang et al., 2012 ).

368 The complex refractive index (RI) of tar aerosols was retrieved under the assumption that the particles have  
369 similar chemical composition and a spherical shape. The SEM images shown in Figure S3 confirm the spherical  
370 morphology and homogeneous composition of the tar ball particles sampled in this study. Electron energy-loss  
371 spectroscopy (EELS) spectra (not shown) indicate that the tar ball particles contain major C and minor O, which  
372 is consistent with the AMS result and previous work (Pósfai et al., 2004; Chakrabarty et al., 2010). Continuous  
373 spectral-dependent RI and SSA for tar ball were derived and are presented in Figure 4, RI results for tar ball  
374 aerosol at mixing ratio of 2:1 and 1:2 are presented in Figure S4. Although scattering dominates the light  
375 extinction, absorption in the UV and in the visible ranges was unambiguously identified for the tar ball aerosols,  
376 with characteristic absorption similar to atmospheric BrC and HULIS (Hoffer et al., 2006; Bluvshstein et al.,  
377 2017; Lin et al., 2017). The imaginary part,  $k$ , increases towards the UV range, presenting 0.02~0.03 difference  
378 over the measured spectra range.  $n$  for the nonpolar tar balls decreased from 1.673 at 365nm to 1.647 at 425nm,  
379 which is almost parallel to the descending  $n$  for the polar tar balls ranging from 1.651 at 365nm to 1.625 at  
380 425nm.  $k$  is 0.029~0.013 for the nonpolar tar ball for light wavelength of 365~425nm, while the imaginary part  
381 for nonpolar aerosols is 0.007 at 365nm and zero at wavelength longer than 410 nm, indicating that there is no  
382 detectable absorption or  $k$  is lower than our detection limit. The nonpolar tar aerosols have stronger light  
383 absorption and relative higher scattering abilities, resulting in a lower SSA compared with the polar tar aerosols.  
384 The SSA increases towards the visible wavelength from 0.86 at 365nm to 0.90 at 425nm for nonpolar tar ball,  
385 and the corresponding values are 0.95 to 1.0 for the polar tar balls.

386 The optical properties of aerosols relate to their chemical composition. Evidently, most of the PAHs identified  
387 in the tar ball aerosols with high intensity have strong absorption between 350 and 450nm, as shown in Figure



388 S5 (Samburova et al., 2016), which coincide the range of tar ball absorption measured here, implying that PAHs  
389 could be a dominate contributor to the absorption of fresh tar balls. Higher imaginary  $k$  can be explained partly  
390 by the larger proportion of PAHs as well as more high-molecular-weight organics present in the nonpolar tar ball  
391 particles, as conjugated aromatic rings and phenols contribute to the major chromophores in the wood smoke  
392 (Laskin et al., 2015). High-molecular weight organics may resemble HULIS that can form charge transfer  
393 complexes (Phillips and Smith, 2004), that can absorb light at a longer wavelength range. The result is  
394 consistent with the finding that higher molecular weight and aromaticity result in stronger absorption for  
395 atmospheric BrC (Dinar et al., 2008). Moreover, the higher NOC content may also contribute to the  
396 chromophores in the nonpolar tar aerosols.

397 The average RIs at 375 and 405 nm are  $1.671+0.025i$  and  $1.659+0.017i$  for nonpolar tar ball aerosols. The  
398 corresponding RIs are  $1.647+0.005i$  and  $1.635+0.04i$  for the polar tar ball aerosols. The imaginary part  $k$   
399 retrieved from the BBCES data, though low, agrees well with  $k$  values calculated from UV-Vis absorption of the  
400 bulk solution. The MAC for the methanol extracts of the fresh tar ball particles is shown in Figure S6. The  
401 absorption may be different for complex materials in the particulate and in the aqueous phases since parameters  
402 such as shape factor, mixing state, together with artifacts from the optical instruments detection and data  
403 retrieval methods can all affect the final optical results, while solvent-dependent extraction/dissolving efficiency  
404 of chromophores or solvent effect (e.g., pH in water solution) may impact the solution absorption coefficient  
405 (Huang et al., 2018; Lin et al., 2017). The light absorption coefficient of particulate BrC has been reported to be  
406 0.7~2.0 times that of bulk BrC extracts by Liu et al. (2013).

407 The absorption Ångström exponent ( $\mathring{A}_{\text{abs}}$ ) is often used to describe the wavelength-dependence of aerosol  
408 light absorption with a value of nearly 1 for BC particles and values substantially larger than 1 indicating the  
409 contribution from BrC (Reid et al., 2005; Chen and Bond, 2010). In this work,  $\mathring{A}_{\text{abs}}$  for nonpolar and polar tar  
410 ball particles ranges from 5.9 to 6.8 between 365 and 425 nm, which is consistent with values of 5.7~7.8  
411 calculated from the bulk absorption measurement. The nonpolar tar balls have a lower  $\mathring{A}_{\text{abs}}$ . The difference in  
412  $\mathring{A}_{\text{abs}}$  reflects the different chemical composition of chromophores in the particles, as inferred also from the AMS  
413 data. Bluvshstein et al. (2017) reported relative low values of  $\mathring{A}_{\text{ext}}$  (2~3) and  $\mathring{A}_{\text{abs}}$  (4~6) over 300~650 nm for  
414 ambient fire plume, which are likely affected by BC present in the smoke aerosol and also due to lower  
415 wavelength dependence of aerosol absorption and scattering over the longwave visible range. Overall, the  
416 broadband optical results for fresh tar ball aerosols are consistent with limited discrete measurements of  
417 atmospheric BBOA as summarized in Table 2. It has also been found that the biomass fuel type, combustion



418 conditions, and atmospheric processing eventually affect the optical properties of BBOA. Lack et al. (2012)  
419 modeled core-shell absorption for primary organic matter (POM) and BC from biomass burning. They found  
420 that the imaginary part of the RI and MAC of POM at 404 nm were  $0.007 \pm 0.005$  and  $0.82 \pm 0.43 \text{ m}^2 \text{ g}^{-1}$ ,  
421 respectively. Charkey et al. (2010) compared the optical properties of tar balls from smoldering combustion of  
422 different biomass. Fuel-dependent imaginary RI for tar ball at 405 nm was  $0.008 \sim 0.015$  and  $\tilde{A}_{\text{abs}}$  over 405–532  
423 nm was 4.2–6.4, which is in line with the  $\tilde{A}_{\text{abs}}$  value of 6–7 reported for BBOA derived HULIS (Hoffer et al.,  
424 2006). Sedlacek et al. (2018) observed a weak absorption for wildfire produced tar balls with RI of  $1.56 + 0.02i$ .  
425 Sumlin et al. (2018) simulated BrC formation under different pyrolysis temperatures. The BrC produced from  
426 over 300 °C combustion has imaginary part of  $k = 0.05 \sim 0.09$  and real part  $n$  of 1.59–1.68 at 375 nm, and RI at  
427 405 nm is  $1.57 + 0.03i$ , corresponded  $\tilde{A}_{\text{abs}}$  over 375–405 nm is 6.4–7.4.

428 Optical mixing rules can be used to estimate or explain the refractive indices of internally mixed substances,  
429 and three mixing rules are commonly applied in climate models: molar refraction of absorption (Jacobson,  
430 2002), volume-weighted linear average of the refractive indices (d'Almeida et al., 1991), and the  
431 Maxwell-Garnett rule (Chýlek et al., 2000). The “linear mixing rule” and molar refraction mixing rules were  
432 tested in this work for mixtures of tar ball particles against the retrieved optical data. Relevant data analysis  
433 details are provided in the supporting materials (Table S3-S4, Figure S7-S11). It was found that both mixing  
434 rules can predict the index of refraction for the polar/nonpolar tar balls, and values calculated based on “linear  
435 mixing rule” fit better with the experimental data.

### 436 3.2 Photooxidation of tar ball particles

437 Aerosols have a wide range of atmospheric lifetimes from hours to days, during which they are involved in  
438 various atmospheric processes, resulting in changes of properties (Reid et al., 2005; Rudich et al., 2007; Jimenez  
439 et al., 2009). Therefore, we studied the effects of photochemical oxidation of the nonpolar wood-pyrolyzed tar  
440 ball aerosols to investigate the physiochemical changes that can occur during tar balls’ atmospheric lifetime.  
441 Figure 5 presents the evolution of the wavelength-dependent RI and SSA as a function of the aerosols’ O:C ratio  
442 following  $\text{NO}_x$ -free photochemical aging in the OFR. The oxidation covers 0.7–6.7 EAD. Substantial decrease of  
443 the RI and an increase of the SSA are correlated with an increase of the O:C ratio. Specific parameters are  
444 summarized in Table S5. Light scattering as well as the absorption by the tar balls aerosol decrease with  
445 increasing OH oxidation. The tar aerosols lose their scattering and absorption significantly up to 3.9 EAD aging.  
446 The average RI decreased from initial  $1.661 + 0.020i$  to  $1.632 + 0.007i$ , and the corresponding average SSA





447 increased from  $0.89 \pm 0.01$  to  $0.96 \pm 0.02$ . Then, the RI by tar balls persisted with enhanced oxidation, so that the  
448 MAC values remained stable after 3.9 days oxidation (Figure S12) suggesting that all the photochemical-labile  
449 chromophores were largely eliminated, while the remaining fraction still presented some light absorption.  
450 Forrister et al. (2015) also observed a stable fraction of biomass burning BrC that had persistent absorption even  
451 after long photochemical evolution time in the ambient environment. They suggested that the remaining  
452 persistent fraction determines the background BrC levels. In our study, the O:C ratio for tar ball aerosols  
453 increased continuously with photochemical oxidation, implying production of oxygenated constituents  
454 (carboxylic, carbonyl compounds, etc.), and the interaction between these increasingly oxidized species coupled  
455 with the relative stable intrinsic chromophoric structures (e.g., fused aromatic rings in Figure 3) in some  
456 supermolecular structure that may explain the persistent absorption for aged tar ball aerosols (Dewar and Lepley,  
457 1961; Desyaterik et al., 2013; Samburova et al., 2016). In addition, a balance between photobleaching of  
458 intrinsic chromophores and photochemical formation of BrC via gas-particle transfer, as well as dynamic  
459 gas-particle partitioning of chromophores and products of their photo-degradation should also be considered in  
460 the overall absorption behavior for BBOA during photochemical processes.

461 The observed photooxidation bleaching is consistent with previous studies on atmospheric processes of BrC.  
462 Sumlin et al. (2017) conducted multiple-day photochemical oxidation on primary biomass burning BrC aerosols  
463 and observed that BrC losses its light absorption and scattering in the near-UV wavelengths by aging. Their  
464 derived RI at 375 nm decreased from  $1.59 \pm 0.03i$  for fresh emission to  $1.50 \pm 0.02i$  after 4.5 EAD oxidation with  
465 a corresponding O:C ratio increase from 0.34 to 0.40. Decrease in the overall BBOA absorption and scattering  
466 was also detected *in-situ* following a one day evolution by Adler et al. (2011). They monitored an average RI of  
467  $1.53 \pm 0.07i$  and  $1.54 \pm 0.04i$  for aerosols dominated by open fire and smoldering emissions, respectively, while  
468 the RI decreased to  $1.49 \pm 0.02i$  of the aged aerosols during the following day. Zhong and Jang (2014) reported  
469 that light absorption of wood smoke BrC was modified by the photochemical process, owing to the production  
470 of BrC from SOA formation and loss of BrC from photochemical bleaching of the chromophores. The total  
471 MAC for the BrC eventually decreased by 19–68% within one day of aging. They proposed that bleaching  
472 occurred by excitation of electrons through the absorption of sunlight via  $\pi-\pi^*$  (UV and near UV illumination)  
473 or  $n-\pi^*$  (visible wavelengths irradiation) transitions. Then, the excited electrons disrupted the conjugated  
474 structure of chromophores, leading to the fading of wood smoke color.

475 When tar ball aerosols were illuminated merely by 254 nm UV light at residence time of 144s, photolysis  
476 occurred, weakly diminished their light absorption, in line with the extent of photon flux exposure. UV



477 irradiation similar to the O<sub>3</sub> condition slightly decreased the average RI to 1.649+0.018i, indicating that  
478 photolysis played a minor role in tar aerosols bleaching and contributed to less than 15% of imaginary k changes  
479 in NO<sub>x</sub>-free photochemical aging process. Even at full power of UV lamps in the OFR, the average RI  
480 decreased by 0.012 and 0.005i for maximum photolyzed aerosols (SI, Table S6-S7, Figure S13-S16). As we also  
481 did not observe detectable optical changes in blank tests upon exposure to O<sub>3</sub> under dark (SI, Figure S17-S18),  
482 the bleaching of the tar balls in the OFR is mainly attributed to OH-initiated chromophores decomposition via  
483 heterogeneous reactions, rather than to O<sub>3</sub> oxidation or photolysis.

484 These results indicate a fundamental relationship between photochemical processes and decreasing light  
485 absorption and scattering in tar ball aerosol as a proxy system for biomass burning BrC aerosols. The changes  
486 are a consequence of chemical composition changes in BrC. These changes occur on a time scale of one daytime  
487 atmospheric aging. In Figure 6a, the H:C, OM/OC,  $\overline{\text{osc}}$ , and particle effective density versus O:C ratio are  
488 shown. Figure 6b presents the contributions of C<sub>x</sub>H<sub>y</sub><sup>+</sup>, C<sub>x</sub>H<sub>y</sub>O<sup>+</sup>, C<sub>x</sub>H<sub>y</sub>O<sub>z</sub><sup>+</sup>, and C<sub>x</sub>H<sub>y</sub>O<sub>i</sub>N<sub>p</sub><sup>+</sup> groups to the tar balls  
489 composition under a range of OH exposure conditions. Mass spectra features and densities of the tar ball  
490 aerosols under various processes are summarized in Table S8. Increasing the OH exposure leads to continuous  
491 increase of O:C and H:C ratios, and higher  $\overline{\text{osc}}$  for the tar balls aerosols. This result is consistent with Sumlin  
492 et al. (2017), who reported that the O:C and H:C for BBOA increased by ~0.08 and ~0.03 after 4.5 EAD  
493 photochemical oxidation, respectively. In this work, the measured O:C ratio increased from 0.25 to 0.38 after  
494 maximum aging, while the H:C ratio increased by 0.07 from initial value of 1.55.

495 Other previous studies also depicted dynamic change of elemental ratios for SOA upon aging (Aiken et al.,  
496 2008). The H:C ratio may either increase or decrease, depending on the precursor type and oxidation conditions.  
497 Overall, O:C and H:C ratios changes relate to specific chemical processes or/and to gas-particle mass transfer  
498 during aging of aerosols (Heald et al., 2010; Kim et al., 2014). The tar ball aerosols consist of mostly reduced  
499 species ( $\overline{\text{osc}} < 0$ ), which oxidize primarily via oxidative formation of polar functional groups to the carbon  
500 skeletons. In OH-initiated oxidation, functionalization includes OH/OOH function group addition and  
501 COOH:Carbonyl groups formation that increase the net oxygen content in SOA (Kroll et al., 2011). Hydration  
502 or polar functional groups addition to unsaturated C-C bonds may also increase the H:C ratio. Moreover,  
503 fragmentation or evaporation also mediate the O:C and H:C ratios of SOA in further aging (Zhang and Seinfeld,  
504 2013; Kim et al., 2014). We attribute the increase in H:C ratio to such oxidation mechanisms that involve bulk  
505 species in the particles. As shown in Table S8,  $f_{m/z>100}$  decreased continuously with aging. After 6.7 EAD  
506 photooxidation,  $f_{m/z>100}$  contributed only 21% of the total organic signals. The decrease of  $f_{m/z>100}$  indicates that



507 fragmentation reactions are involved in the photochemical evolution and decomposition of high-molecular  
508 weight compounds, thereby, reducing the size of the conjugated molecular system. The persistent high value of  
509  $f_{m/z>100}$  after 6.7 EAD photooxidation imply that some high molecular weight compounds remained in the tar ball  
510 aerosols, and continue to contribute to light absorption either as individual chromophores or as charge transfer  
511 complexes. Figure 6b shows that while  $C_xH_y^+$  fragments deplete with OH exposure,  $C_xH_yO^+$  and  $C_xH_yO_2^+$   
512 fragments increase, implying the formation of oxygenated moieties in the tar ball aerosols. In addition, a  
513 decrease in the  $C_xH_yO_iN_p^+$  fraction was measured from initial 3.6% to 1.9% after maximum oxidation. Ng et al.  
514 (2010) suggested to use  $f_{44}(CO_2^+)$  vs.  $f_{43}(C_2H_3O^+)$  triangle space as indication of OA sources and for estimation  
515 of their degree of oxidation and volatility. The  $C_2H_3O^+$  (less oxidized fragments) indicate aldehydes or ketones.  
516 High  $f_{44}/f_{43}$  ratio indicates low volatility and high oxidation level of SOA. Moreover, high  $f_{44}/f_{43}$  and O:C  
517 ratio are associated with increased hygroscopicity and possible CCN activity of OA (Hennigan et al., 2011;  
518 Lambe et al., 2011). The  $f_{44}$  vs.  $f_{43}$  in this study varied with photochemical aging and fell within the expected  
519 range for ambient OOA, as shown in Figure 7. Increase of  $f_{44}/f_{43}$  ratio with OH oxidation in Figure 6(b)  
520 depicted the increase of carboxylic and/or peroxide compounds compared to carbonyl species in the tar balls,  
521 which is consistent with the atmospheric evolution of ambient biomass burning plumes (Hennigan et al., 2011;  
522 Canonaco et al., 2015).

523 To infer the possible chemical processes, detailed mass spectra of tar aerosols upon 6.7 EAD photochemical  
524 oxidation were compared to a fresh ones (Figure S19). We found that decrease of alkyl/alkenyl chains (e.g.,  
525  $C_nH_{2n-1}^+$ ,  $C_nH_{2n+1}^+$ ) and aromatic ring structure fragments (e.g.,  $C_6H_5^+$ ,  $C_6H_9^+$ ) contributed the prominent changes  
526 in the  $C_xH_y^+$  group, and relative higher  $CO_2^+$  increment relative to  $C_2H_3O^+$  explained the increase in the  $f_{44}/f_{43}$   
527 ratio. The decrease in the abundance of  $C_2H_4O_2^+$  ( $m/z$  60) and  $C_3H_5O_2^+$  ( $m/z$  73) is consistent with recent studies  
528 that levoglucosan or similar species can decay in the atmosphere due to photochemical oxidation (Hennigan et  
529 al., 2010). The pronounced decrease of intensity at  $m/z$  137 ( $C_8H_9O_2^+$  and  $C_7H_5O_3^+$ ) suggests that the  
530 methoxy-phenol components in tar balls depleted substantially upon maximal aging.

531 In summary, photochemical oxidation by OH radicals destructed the aromatic rings and methoxy phenolic  
532 structures, which are expected to be the primary chromophores in the tar balls. The NOC content and  
533 high-molecular weight species also depleted via OH oxidation. These chemical changes upon OH oxidation may  
534 explain the observed diminishing in light scattering and absorption upon photochemical aging.

### 535 3.3 $NO_x$ -dependent tar ball particles oxidation



536 N<sub>2</sub>O was recently introduced for simulating NO<sub>x</sub>-dependent SOA formation pathways in OFR under high O<sub>3</sub>  
537 concentration, as O(<sup>1</sup>D)+N<sub>2</sub>O reactions can be applied to systematically vary the branching ratio of the RO<sub>2</sub>+NO  
538 reactions relative to the RO<sub>2</sub>+HO<sub>2</sub> and/or RO<sub>2</sub>+RO<sub>2</sub> reactions over a range of conditions relevant to atmospheric  
539 SOA formation (Lambe et al., 2017). Here we introduced 0.5 and 2.0 vol.% N<sub>2</sub>O to investigate NO<sub>x</sub>-involved  
540 daytime aging of tar ball aerosols in the OFR. The OH exposures were maintained for all these tests at about 4  
541 EAD. The NO<sub>2</sub> concentrations downstream of the OFR was measured to be 96.1±1.3 and 528.3±6.2 ppbv. The  
542 concentration of static NO can be neglected under these oxidation conditions. Figure 8 shows the mass spectra  
543 features for fresh and aged tar balls reacted in the absence/presence of NO<sub>x</sub>. Parameters including organic  
544 elemental ratios and densities are summarized in Table S8. In general, tar aerosols oxidized under N<sub>2</sub>O addition  
545 exhibit higher O:C and relative lower H:C ratios. NO<sub>y</sub><sup>+</sup> (NO<sup>+</sup> and NO<sub>2</sub><sup>+</sup>) signals appear in the mass spectra and  
546 the intensities of NO<sub>y</sub><sup>+</sup> display a positive trend with N<sub>2</sub>O concentration, together with an increase of oxygenated  
547 fragments (C<sub>x</sub>H<sub>y</sub>O<sup>+</sup> and C<sub>x</sub>H<sub>y</sub>O<sub>z</sub><sup>+</sup>). The normalized fractions of hydrocarbon fragments (C<sub>x</sub>H<sub>y</sub><sup>+</sup>) slightly  
548 decreased. The signal ratio of NO<sup>+</sup> (*m/z* 30) to NO<sub>2</sub><sup>+</sup> (*m/z* 46) is used to distinguish organic nitrate from  
549 inorganic nitrate. The signal from standard inorganic nitrate (e.g., NH<sub>4</sub>NO<sub>3</sub>) has a typical NO<sub>2</sub><sup>+</sup>/NO<sup>+</sup> ratio of  
550 0.485 using our AMS (detailed mass spectrum is shown in Figure S20), similar to previous studies (Zhou et al.,  
551 2017). The fraction of NO<sub>y</sub><sup>+</sup> (NO<sup>+</sup> and NO<sub>2</sub><sup>+</sup>) signals in the aged tar aerosols increased from 0% to 0.7% and  
552 1.5% at 0.5 vol.% and 2.0 vol.% N<sub>2</sub>O additions, respectively. The corresponding values of NO<sub>2</sub><sup>+</sup>/NO<sup>+</sup> ratio are  
553 0.162 and 0.174, which are lower than that for inorganic nitrates. In addition, the contribution of C<sub>x</sub>H<sub>y</sub>O<sub>i</sub>N<sub>p</sub><sup>+</sup>  
554 fragments increased from 1.9% to 4.4% and 4.5% over the course of aging. Therefore, we conclude that NOC  
555 rather than inorganic nitrate formed in the NO<sub>x</sub>-dependent photooxidation process, resulting in an overall  
556 increase of N:C ratio from 0.010 to 0.012 and 0.015. Additionally, the density of tar balls weakly increased from  
557 1.24 to 1.26 with 2.0% N<sub>2</sub>O addition.

558 Detailed changes in the mass spectra over the course of the experiment are shown in Figure S21. Ions  
559 indicative of cyclolakyl fragments (e.g., C<sub>2</sub>H<sub>3</sub><sup>+</sup>, C<sub>3</sub>H<sub>5</sub><sup>+</sup>, C<sub>4</sub>H<sub>7</sub><sup>+</sup>) decreased, while NO<sub>x</sub> addition increased the CO<sup>+</sup>  
560 and CO<sub>2</sub><sup>+</sup> intensities relative to C<sub>2</sub>H<sub>3</sub>O<sup>+</sup>, leading to higher *f*<sub>44</sub>/*f*<sub>43</sub> ratio. Ng et al. (2007) observed a similar  
561 change for photooxidation of terpenes in presence of NO<sub>x</sub>. Changes of AMS spectra with NO<sub>x</sub> addition may  
562 mark differences between the dominating reaction pathways in tar ball photooxidation as RO<sub>2</sub>+NO verses  
563 RO<sub>2</sub>+HO<sub>2</sub> and/or RO<sub>2</sub>+RO<sub>2</sub> reactions.

564 Photochemical oxidation with NO<sub>x</sub> addition enhances the oxidation level and increases the absorption and  
565 scattering of tar ball aerosols. Dynamic changes of the complex RI are shown in Figure 9 and summarized in



566 Table S5. The RI of tar ball aerosols increased from an average of  $1.632+0.007i$  for pure OH-initiated  
567 photooxidation to  $1.635+0.015i$  with the addition of 0.5 vol.%  $N_2O$ , and a greater increase up to  $1.648+0.019i$   
568 with 2.0 vol.%  $N_2O$ . The increase of RI is therefore primarily attributed to NOC formation. Zhong and Jang  
569 (2014) observed that higher  $NO_x$  level slowed photo-bleaching of wood smoke BrC, and they suggested that  
570  $NO_x$ -modified reaction pathways produce secondary NOC chromophores (i.e., nitro-phenols). Liu et al. (2016)  
571 simulated daytime chemistry of various VOCs in the presence of  $NO_x$  and found that light absorption of  
572 produced SOA, especially aromatic ones, increased with  $NO_x$  concentration. These findings were also  
573 corroborated by experimental study of Lin et al. (2015), where the chemical composition and the light  
574 absorption properties of laboratory generated toluene SOA were reported to have strong positive dependence on  
575 the presence of nitro-phenols formed at high  $NO_x$  oxidation conditions. The color of the BrC diminished with  
576 photolysis, correlated with a decline of the NOC fraction. Nitration of aromatic species via  $NO_x/N_2O_5/NO_3$  has  
577 been proposed as one of the main mechanisms to produce secondary BrC in the atmosphere (Lu et al., 2011; Lin  
578 et al., 2015, 2017; Bluvshstein et al., 2017).

579 The imaginary part at 2.0 vol. %  $N_2O$  addition was almost comparable with that of the fresh tar aerosols  
580 (average value:  $RI=1.661+0.020i$ ), although the real part was lower, suggesting that photooxidation in the  
581 presence of  $NO_x$  promote the formation of N-containing chromophores via secondary processes. In our  
582 experiments, formation of the N-containing chromophores overweighed the bleaching from OH photooxidation  
583 to eventually regain the absorption of aged tar balls. The SSA calculated for 150 nm particles decreased from  
584 0.96 to 0.91 and 0.89 with  $N_2O$  addition. Absorption enhancement with  $N_2O$  addition for tar balls upon  
585 photooxidation can also be seen in the MAC changes shown in Figure S22, where MAC at 375 nm for fresh tar  
586 ball was  $0.854 \text{ m}^2 \text{ g}^{-1}$ , it decreased to  $0.416 \text{ m}^2 \text{ g}^{-1}$  via OH photo-bleaching, then MAC increased to  $0.459 \text{ m}^2 \text{ g}^{-1}$   
587 at 0.5 vol.%  $N_2O$  addition, and up to  $0.598 \text{ m}^2 \text{ g}^{-1}$  at 2.0 vol.%  $N_2O$  addition due to chromophores formation.

### 588 3.4 Atmospheric and Climate implication

589 Atmospheric aging alters the RI of SOA, and the dynamic changes of RI depend on complicated reaction  
590 pathways (Liu et al., 2016). OH-initiated photochemical oxidation and photolysis decrease the RI of laboratory  
591 proxies of tar balls under  $NO_x$ -free condition, while photooxidation under high  $NO_x$  has an opposite effect on  
592 the RI of tar balls aerosol. We investigated the relationship between the dynamic RI values of tar ball particles  
593 and their possible climatic implications, including the change of light extinction/absorption efficiency and the  
594 clear-sky direct radiative forcing. For clarity, light extinction/absorption efficiencies were calculated and



595 compared at wavelength of 375 and 405 nm, while radiative forcing was estimated over all the measured  
596 wavelengths from 365 to 425 nm. Atmospheric and climatic implications were assessed for fresh and oxidized  
597 tar ball upon NO<sub>x</sub>-dependent ~3.9 EDA photooxidation (O<sub>3.9</sub>, N<sub>0.5</sub>, and N<sub>2.0</sub>), in which fresh tar balls  
598 were taken as reference.

599 As shown in Figure 10, photochemical oxidation under NO<sub>x</sub>-free condition (O<sub>3.9</sub>) diminished light  
600 extinction and absorption efficiency of tar balls aerosols in the atmospheric relevant size of 50-300 nm, causing  
601 about 5~40% decrease in extinction at 375 and 405 nm wavelength. For aerosols larger than 400 nm, the  
602 extinction efficiency of tar ball aerosols increased instead after photochemical aging. The light extinction  
603 efficiency presented higher size-dependence than absorption, and extinction changes were more sensitive to  
604 particle size, especially in the smaller sizes. The decreased absorption was more pronounced with ~60%  
605 decrease at 375 nm and over 75% at 405 nm. Previous studies have confirmed the relationship between biomass  
606 burning emissions and acute regional visibility deterioration (Huang et al., 2012; Chen et al., 2017). Our results  
607 demonstrate that OH radical initiated daytime aging may play an important role in improving visibility  
608 degradation caused by primary biomass BrC. However, photochemical evolution under high NO<sub>x</sub> conditions  
609 may compensate effects of the photooxidation bleaching of tar ball aerosols via the formation of NOC  
610 chromophores. At N<sub>0.5</sub> conditions, the light extinction decreased by 4 to 20% at 375 nm and 5 to 24% at 405  
611 nm, respectively. The corresponding absorption decrease was 20~27% at both wavelengths. With more N<sub>2</sub>O  
612 addition, formation of secondary N-containing chromophores almost completely offsets light  
613 extinction/absorption decrease caused by photooxidation. Under the N<sub>2.0</sub> conditions, enhancement of light  
614 absorption efficiency for tar ball was about 0~9% at 405 nm in the entire size range of 50-500 nm.

615 Radiative forcing from aerosols over both ground and snow is vital to climate models (Barnett et al., 2005;  
616 Kanakidou et al., 2005). Integrated radiative forcing for tar ball aerosols as a function of particle size under  
617 various oxidation conditions is shown in Figure 11. Size-/wavelength-resolved SRF are also shown in Figure  
618 S23 and S24. Integrated SRF over ground has negative values for tar balls over almost all the atmospheric  
619 relevant sizes, indicating a radiative cooling effect by tar ball aerosols except at 195~210 nm, where fresh tar  
620 ball particles present warming effect with SRF up to ~0.48 W g<sup>-1</sup>. In practical fire emissions, the size of tar balls  
621 depends on the burning and environment conditions and biomass fuel types with typical values between tens to  
622 hundreds of nanometers (Reid et al., 2005; Pósfai et al., 2004). The complicated size-dependence character of  
623 SRF makes it difficult to assess the real climatic effect of tar ball particles without extensive calculations. Figure  
624 11(a) suggests fresh tar balls have SRF values of -7.46 W g<sup>-1</sup> at 150 nm and 0.45 W g<sup>-1</sup> at 200 nm, respectively.



625 The SRF decreased for all size ranges due to photochemical oxidation to  $-7.93 \text{ W g}^{-1}$  at 150 nm and  $-1.37 \text{ W g}^{-1}$   
626 at 200 nm for tar ball aerosols under O<sub>3</sub> condition. At N<sub>0.5</sub> conditions, SRF was  $-7.37 \text{ W g}^{-1}$  at 150 nm and  
627  $0.16 \text{ W g}^{-1}$  at 200 nm, and the corresponding values at N<sub>2.0</sub> conditions increased to  $-7.20 \text{ W g}^{-1}$  at 150 nm and  
628  $0.31 \text{ W g}^{-1}$  at 200 nm.

629 In contrast, tar ball particles contributed to positive forcing (warming effect) over the bright terrain  
630 throughout the atmospheric aging, as shown in Figure 11(b). Radiative forcing over the snow showed a simple  
631 increasing trend with particle size, indicating that larger BrC aerosol with identical mass loading in the air have  
632 a higher warming effect. The changes of snow-based radiative forcing upon photochemical aging followed the  
633 same trends as in the ground-based cases. Fresh tar ball at size of 200 nm has SRF of  $20.12 \text{ W g}^{-1}$  over the  
634 incident solar wavelength of 365–425 nm on the snow terrain. With photochemical oxidation under NO<sub>x</sub>-free  
635 condition, radiative forcing decreased significantly. After 3.9 EAD atmospheric aging, snow-based radiative  
636 forcing for tar ball decreased by 65–73% over the size range of 50–500 nm, the value of 200 nm tar ball became  
637  $6.99 \text{ W g}^{-1}$ . When NO<sub>x</sub> was involved in the photochemical oxidation of tar balls, the decrement of radiative  
638 forcing was weakened. At N<sub>0.5</sub>, SRF for 200 nm tar ball was  $14.01 \text{ W g}^{-1}$ , while at N<sub>2.0</sub> condition,  
639 size-dependent SRF from the aged tar ball was almost comparable with that from fresh tar ball, and SRF for 200  
640 nm tar ball was  $18.56 \text{ W g}^{-1}$ .

641 Although less than 10% of the solar spectrum's energy is distributed between 365 and 425 nm, the radiative  
642 forcing over this range represents a significant warming or cooling potential over the arctic terrain. In  
643 conclusion, photochemical oxidation under NO<sub>x</sub>-free conditions can decrease radiative forcing of tar ball  
644 aerosols, resulting in enhancement in the cooling effect over ground and decreased in warming effect over the  
645 snow. However, NO<sub>x</sub> involvement in photooxidation inhibits the decrease in radiative forcing of tar ball  
646 aerosols. Overall, the complex changes in optical properties of tar balls at long aging times impose great  
647 uncertainties in traditional model-based estimation of BBOA. Our study emphasizes the importance of taking  
648 this atmospheric process into consideration to refine the understanding of the climatic and atmospheric  
649 influences from these aerosols.

#### 650 4 Conclusions

651 In this study, proxies for tar ball aerosols were generated in the laboratory following a flameless wood pyrolysis  
652 process. The optical and chemical properties of the generated tar balls were constrained using BBCES and  
653 HiRes-Tof-AMS/SP-LD-REMPI-MS and were shown to have many similarities to ambient biomass burning



654 aerosols. Laboratory generated fresh tar ball aerosols have light absorption characteristics similar to atmospheric  
655 BrC with higher absorption efficiency towards the UV. The average complex refractive indices between 365 and  
656 425 nm are  $1.661+0.020i$  and  $1.635+0.003i$  for nonpolar and polar tar ball aerosols, respectively.

657 Atmospheric evolution for tar ball aerosols was experimentally simulated using an oxidation flow reactor. The  
658 study focused on dynamic changes in the optical and chemical properties due to NO<sub>x</sub>-dependent photochemical  
659 oxidation. Furthermore, the relationship between oxidation level and the resulting RI of the tar ball aerosols was  
660 explored. We found a substantial decrease in the scattering and absorption properties of tar balls, with a  
661 corresponding increase in SSA with OH oxidation in the absence of NO<sub>x</sub>. A correlation between the RI decrease  
662 and increase in the O:C and H:C ratios was observed. The decrease in light scattering and absorption is  
663 attributed to the destruction of aromatic/phenolic/NOC and high-molecular weight species chromophores via  
664 OH-initiated photooxidation of tar balls. Over longer aging times, the average RI of the tar ball aerosols  
665 decreased from  $1.661+0.020i$  to  $1.632+0.007i$  upon atmospheric equivalent to 3.9 days aging, and the  
666 corresponding O:C and H:C ratio increased from initial 0.25 and 1.55 to 0.35 and 1.59, respectively.

667 Our results suggest that OH oxidation rather than photolysis or ozone reactions plays the dominate role that  
668 determine the optical and chemical properties in tar balls aging. The observed decrease in absorption results  
669 from depletion of chromophores such as aromatic rings, phenolic compounds and high molecular weights  
670 species.

671 Simulations under high NO<sub>x</sub> environment enhanced the aerosol oxidation state and increased the scattering  
672 and absorption of tar ball aerosols relative to OH photooxidation in the absence of NO<sub>x</sub>. At ~3.9 EAD, addition  
673 of 0.5 and 2.0 vol.% N<sub>2</sub>O increased the organic elemental ratios (O:C, H:C, and N:C ratios) and doubled the  
674 organic nitrates fraction in the particles from 1.9 % to ~4.4 %. The formation of NOC chromophores overweigh  
675 the intrinsic depletion of chromophores, leading to higher RI of  $1.635+0.015i$  and  $1.648+0.019i$ .

676 The atmospheric and climatic implications from tar ball aerosols under various oxidation conditions were  
677 assessed using a simple radiative forcing model in terms of extinction/absorption efficiency changes and  
678 ground-/snow-based radiative forcing. These results demonstrate that the optical and chemical properties of tar  
679 ball particles are dynamically related to atmospheric aging, and optical changes are governed by both  
680 photobleaching and secondary chromophores formation. Therefore, the atmospheric process should be  
681 emphasized in model predictions for evaluating biomass burning BrC aerosol radiative forcing as well as  
682 climate change.

683





684 **Acknowledgments**

685 This research was partially supported by research grants from the US-Israel Binational Science Foundation  
686 (BSF) grant no. 2016093 and Israel Ministry of Science, Maimonide program. Dr. Li acknowledges support  
687 from the Planning & Budgeting Committee, Israel (2018/19). J. Schade, J. Passig and R. Zimmermann  
688 gratefully acknowledge financial support from the German Research Foundation, project number ZI 764/6-1,  
689 and Photonion GmbH, Schwerin, Germany.



690 **Reference**

- 691 Abo Riziq, A., Erlick, C., Dinar, E., and Rudich, Y.: Optical properties of absorbing and non-absorbing aerosols  
692 retrieved by cavity ring down (CRD) spectroscopy, *Atmos. Chem. Phys.*, 7, 1523-1536,  
693 doi:10.5194/acp-7-1523-2007, 2007.
- 694 Adler, G., Riziq, A. A., Erlick, C., and Rudich, Y.: Effect of intrinsic organic carbon on the optical properties of  
695 fresh diesel soot, *P. Natl. Acad. Sci. USA*, 107, 6699-6704, doi:10.1073/pnas.0903311106, 2010.
- 696 Adler, G., Flores, J. M., Abo Riziq, A., Borrmann, S., and Rudich, Y.: Chemical, physical, and optical evolution  
697 of biomass burning aerosols: a case study, *Atmos. Chem. Phys.*, 11, 1491-1503, doi:10.5194/acp-11-1491-2011,  
698 2011.
- 699 Aiken, A. C., Decarlo, P. F., Kroll, J. H., Worsnop, D. R., Huffman, J. A., Docherty, K. S., Ulbrich, I. M., Mohr,  
700 C., Kimmel, J. R., and Sueper, D.: O/C and OM/OC ratios of primary, secondary, and ambient organic aerosols  
701 with high-resolution time-of-flight aerosol mass spectrometry, *Environ. Sci. Technol.*, 42, 4478-4485,  
702 doi: 10.1021/es703009q, 2008.
- 703 Alexander, D. T., Crozier, P. A., and Anderson, J. R.: Brown carbon spheres in East Asian outflow and their  
704 optical properties, *Science*, 321, 833-836, doi: 10.1126/science.1155296, 2008.
- 705 Andreae, M. O. and Gelencsér, A.: Black carbon or brown carbon? The nature of light-absorbing carbonaceous  
706 aerosols, *Atmos. Chem. Phys.*, 6, 3131-3148, doi:10.5194/acp-6-3131-2006, 2006.
- 707 Bahadur, R., Praveen, P. S., Xu, Y., and Ramanathan, V.: Solar absorption by elemental and brown carbon  
708 determined from spectral observations, *P. Natl. Acad. Sci. USA*, 201205910, doi:10.1073/pnas.1205910109,  
709 2012.
- 710 Barnett, T. P., Adam, J. C., and Lettenmaier, D. P.: Potential impacts of a warming climate on water availability  
711 in snow-dominated regions, *Nature*, 438, 303-309, doi:10.1038/nature04141, 2005.
- 712 Bente, M., Sklorz, M., Streibel, T., and Zimmermann, R.: Online laser desorption-multiphoton postionization  
713 mass spectrometry of individual aerosol particles: molecular source indicators for particles emitted from  
714 different traffic-related and wood combustion sources, *Anal. Chem.*, 80, 8991-9004, doi: 10.1021/ac801295f,  
715 2008.
- 716 Bente, M., Sklorz, M., Streibel, T., and Zimmermann, R.: Thermal desorption-multiphoton ionization  
717 time-of-flight mass spectrometry of individual aerosol particles: A simplified approach for online single-particle



- 718 analysis of Polycyclic Aromatic Hydrocarbons and their derivatives, *Anal. Chem.*, 81, 2525-2536,  
719 doi: 10.1021/ac802296f, 2009.
- 720 Bluvshstein, N., Lin, P., Flores, J. M., Segev, L., Mazar, Y., Tas, E., Snider, G., Weagle, C., Brown, S. S., and  
721 Laskin, A.: Broadband optical properties of biomass-burning aerosol and identification of brown carbon  
722 chromophores, *J. Geophys. Res. Atmos.* 122, 5441-5456, doi:10.1002/2016JD026230, 2017.
- 723 Boesl, U., Neusser, H., and Schlag, E.: Two-photon ionization of polyatomic molecules in a mass spectrometer,  
724 *Zeitschrift für Naturforschung A*, 33, 1546-1548, doi: <https://doi.org/10.1515/zna-1978-1218>, 1978.
- 725 Bond, T. C., and Bergstrom, R. W.: Light absorption by carbonaceous particles: An investigative review, *Aerosol*  
726 *Sci. Tech.*, 40, 27-67, doi:10.1080/02786820500421521, 2006.
- 727 Canonaco, F., Slowik, J., Baltensperger, U., and Prévôt, A.: Seasonal differences in oxygenated organic aerosol  
728 composition: implications for emissions sources and factor analysis, *Atmos. Chem. Phys.*, 15, 6993-7002,  
729 doi:10.5194/acp-15-6993-2015, 2015.
- 730 Chakrabarty, R., Moosmüller, H., Chen, L. W., Lewis, K., Arnott, W., Mazzoleni, C., Dubey, M., Wold, C., Hao,  
731 W., and Kreidenweis, S.: Brown carbon in tar balls from smoldering biomass combustion, *Atmos. Chem. Phys.*,  
732 10, 6363-6370, doi:10.5194/acp-10-6363-2010, 2010.
- 733 Chen, Y., and Bond, T.: Light absorption by organic carbon from wood combustion, *Atmos. Chem. Phys.*, 10,  
734 1773-1787, doi:10.5194/acp-10-1773-2010, 2010.
- 735 Chen, J., Li, C., Ristovski, Z., Milic, A., Gu, Y., Islam, M. S., Wang, S., Hao, J., Zhang, H., and He, C.: A review  
736 of biomass burning: Emissions and impacts on air quality, health and climate in China, *Sci. Total Environ.*, 579,  
737 1000-1034, doi:10.1016/j.scitotenv.2016.11.025, 2017
- 738 Chýlek, P., Videen, G., Geldart, D., Dobbie, J. S., and Tso, H.: Effective medium approximations for  
739 heterogeneous particles, *Light scattering by nonspherical particles: theory, measurements, and applications*, pp.  
740 273-308, edited by: Mishchenko, M. I., Hovenier, J. W., and Travis, L. D., Academic Press, 2000.
- 741 Czech, H., Pieber, S. M., Tiitta, P., Sippula, O., Kortelainen, M., Lamberg, H., Grigonyte, J., Streibel, T., Prévôt,  
742 A. S., and Jokiniemi, J.: Time-resolved analysis of primary volatile emissions and secondary aerosol formation  
743 potential from a small-scale pellet boiler, *Atmos. Environ.*, 158, 236-245, doi:10.1016/j.atmosenv.2017.03.040,  
744 2017.
- 745 d'Almeida, G. A., Koepke, P., and Shettle, E. P.: *Atmospheric aerosols: global climatology and radiative*  
746 *characteristics*, A. Deepak Publishing, Hampton, Va, 1991.



- 747 DeCarlo, P. F., Kimmel, J. R., Trimborn, A., Northway, M. J., Jayne, J. T., Aiken, A. C., Gonin, M., Fuhrer, K.,  
748 Horvath, T., and Docherty, K. S.: Field-deployable, high-resolution, time-of-flight aerosol mass spectrometer,  
749 Anal. Chem., 78, 8281-8289, doi:10.1021/ac061249n, 2006.
- 750 Desyaterik, Y., Sun, Y., Shen, X., Lee, T., Wang, X., Wang, T., and Collett, J. L.: Speciation of “brown” carbon  
751 in cloud water impacted by agricultural biomass burning in eastern China, J. Geophys. Res. Atmos., 118,  
752 7389-7399, doi:10.1002/jgrd.50561, 2013.
- 753 Dewar, M. J., and Lepley, A. R.:  $\pi$ -Complexes. I. Charge Transfer Spectra of  $\pi$ -Complexes Formed by  
754 Trinitrobenzene with Polycyclic Aromatic Compounds<sup>1</sup>, J. Am. Chem. Soc., 83, 4560-4563, 1961.
- 755 Dinar, E., Riziq, A. A., Spindler, C., Erlick, C., Kiss, G., and Rudich, Y.: The complex refractive index of  
756 atmospheric and model humic-like substances (HULIS) retrieved by a cavity ring down aerosol spectrometer  
757 (CRD-AS), Faraday Discuss., 137, 279-295, doi:10.1039/B703111D, 2008.
- 758 Epstein, S. A., Blair, S. L., and Nizkorodov, S. A.: Direct photolysis of  $\alpha$ -pinene ozonolysis secondary organic  
759 aerosol: effect on particle mass and peroxide content, Environ. Sci. Technol., 48, 11251-11258,  
760 doi:10.1021/es502350u, 2014.
- 761 Feng, Y., Ramanathan, V., and Kotamarthi, V.: Brown carbon: a significant atmospheric absorber of solar  
762 radiation?, Atmos. Chem. Phys., 13, 8607-8621, doi:10.5194/acp-13-8607-2013, 2013.
- 763 Finewax, Z., de Gouw, J. A., and Ziemann, P. J.: Identification and quantification of 4-Nitrocatechol formed  
764 from OH and NO<sub>3</sub> radical-initiated reactions of catechol in air in the presence of NOx: Implications for  
765 secondary organic aerosol formation from biomass burning, Environ. Sci. Technol., 52, 1981-1989,  
766 doi:10.1021/acs.est.7b05864, 2018.
- 767 Flores, J., Zhao, D., Segev, L., Schlag, P., Kiendler-Scharr, A., Fuchs, H., Watne, Å., Bluvshstein, N., Mentel, T.  
768 F., and Hallquist, M.: Evolution of the complex refractive index in the UV spectral region in ageing secondary  
769 organic aerosol, Atmos. Chem. Phys., 14, 5793-5806, doi:10.5194/acp-14-5793-2014, 2014a.
- 770 Flores, J. M., Washenfelder, R., Adler, G., Lee, H., Segev, L., Laskin, J., Laskin, A., Nizkorodov, S., Brown, S.,  
771 and Rudich, Y.: Complex refractive indices in the near-ultraviolet spectral region of biogenic secondary organic  
772 aerosol aged with ammonia, Phys. Chem. Chem. Phys., 16, 10629-10642, doi:10.1039/C4CP01009D, 2014b.
- 773 Flowers, B., Dubey, M., Mazzoleni, C., Stone, E., Schauer, J., Kim, S. W., and Yoon, S.:  
774 Optical-chemical-microphysical relationships and closure studies for mixed carbonaceous aerosols observed at  
775 Jeju Island; 3-laser photoacoustic spectrometer, particle sizing, and filter analysis, Atmos. Chem. Phys., 10,  
776 10387-10398, doi:10.5194/acp-10-10387-2010, 2010.



- 777 Forrister, H., Liu, J., Scheuer, E., Dibb, J., Ziemba, L., Thornhill, K. L., Anderson, B., Diskin, G., Perring, A. E.,  
778 and Schwarz, J. P.: Evolution of brown carbon in wildfire plumes, *Geophys. Res. Lett.*, 42, 4623-4630,  
779 doi:10.1002/2015GL063897, 2015.
- 780 Forster, P. M. F., and Taylor, K. E.: Climate forcings and climate sensitivities diagnosed from coupled climate  
781 model integrations, *J. Clim.*, 19, 6181-6194, doi:10.1175/JCLI3974.1, 2006.
- 782 Fu, H., Zhang, M., Li, W., Chen, J., Wang, L., Quan, X., and Wang, W.: Morphology, composition and mixing  
783 state of individual carbonaceous aerosol in urban Shanghai, *Atmos. Chem. Phys.*, 12, 693-707,  
784 doi:10.5194/acp-12-693-2012, 2012.
- 785 Ge, X., Setyan, A., Sun, Y., and Zhang, Q.: Primary and secondary organic aerosols in Fresno, California during  
786 wintertime: Results from high resolution aerosol mass spectrometry, *J. Geophys. Res. Atmos.*, 117, D19301,  
787 doi:10.1029/2012JD018026, 2012.
- 788 Grottemeyer, J., Boesl, U., Walter, K., and Schlag, E. W.: A general soft ionization method for mass spectrometry:  
789 Resonance-enhanced multi-photon ionization of biomolecules, *Org. Mass. Spectrom.*, 21, 645-653,  
790 doi:10.1002/oms.1210211008, 1986.
- 791 Hand, J. L., Malm, W., Laskin, A., Day, D., Lee, T. B., Wang, C., Carrico, C., Carrillo, J., Cowin, J. P., and  
792 Collett, J.: Optical, physical, and chemical properties of tar balls observed during the Yosemite Aerosol  
793 Characterization Study, *J. Geophys. Res. Atmos.*, 110, D21210, doi:10.1029/2004JD005728, 2005.
- 794 He, L. Y., Lin, Y., Huang, X. F., Guo, S., Xue, L., Su, Q., Hu, M., Luan, S. J., and Zhang, Y. H.: Characterization  
795 of high-resolution aerosol mass spectra of primary organic aerosol emissions from Chinese cooking and biomass  
796 burning, *Atmos. Chem. Phys.*, 10, 11535-11543, doi:10.5194/acp-10-11535-2010, 2010.
- 797 Heald, C., Kroll, J., Jimenez, J., Docherty, K., DeCarlo, P., Aiken, A., Chen, Q., Martin, S., Farmer, D., and  
798 Artaxo, P.: A simplified description of the evolution of organic aerosol composition in the atmosphere,  
799 *Geophys. Res. Lett.*, 37, L08803, doi:10.1029/2010GL042737, 2010.
- 800 Hennigan, C., Miracolo, M., Engelhart, G., May, A., Presto, A., Lee, T., Sullivan, A., McMeeking, G., Coe, H.,  
801 and Wold, C.: Chemical and physical transformations of organic aerosol from the photo-oxidation of open  
802 biomass burning emissions in an environmental chamber, *Atmos. Chem. Phys.*, 11, 7669-7686,  
803 doi:10.5194/acp-11-7669-2011, 2011.
- 804 Hennigan, C. J., Sullivan, A. P., Collett Jr, J. L., and Robinson, A. L.: Levoglucosan stability in biomass burning  
805 particles exposed to hydroxyl radicals, *Geophys. Res. Lett.*, 37, L09806, doi:10.1029/2010GL043088, 2010.



- 806 He, Q., Bluvshstein, N., Segev, L., Meidan, D., Flores, J. M., Brown, S. S., Brune, W., and Rudich, Y.: Evolution  
807 of the complex refractive index of secondary organic aerosols during atmospheric aging, *Environ. Sci. Technol.*,  
808 52, 3456-3465, doi:10.1021/acs.est.7b05742, 2018.
- 809 Heger, H. J., Zimmermann, R., Dorfner, R., Beckmann, M., Griebel, H., Kettrup, A., and Boesl, U.: On-line  
810 emission analysis of polycyclic aromatic hydrocarbons down to pptv concentration levels in the flue gas of an  
811 incineration pilot plant with a mobile resonance-enhanced multiphoton ionization time-of-flight mass  
812 spectrometer, *Anal. Chem.*, 71, 46-57, doi:10.1021/ac980611y, 1999.
- 813 Herring, C. L., Faiola, C. L., Massoli, P., Sueper, D., Erickson, M. H., McDonald, J. D., Simpson, C. D., Yost, M.  
814 G., Jobson, B. T., and VanReken, T. M.: New methodology for quantifying polycyclic aromatic hydrocarbons  
815 (PAHs) using high-resolution aerosol mass spectrometry, *Aerosol Sci. Tech.*, 49, 1131-1148,  
816 doi:10.1080/02786826.2015.1101050, 2015.
- 817 Hoffer, A., Gelencsér, A., Guyon, P., Kiss, G., Schmid, O., Frank, G., Artaxo, P., and Andreae, M.: Optical  
818 properties of humic-like substances (HULIS) in biomass-burning aerosols, *Atmos. Chem. Phys.*, 6, 3563-3570,  
819 doi: 10.5194/acp-6-3563-2006, 2006.
- 820 Hoffer, A., Tóth, A., Nyiró-Kósa, I., Pósfai, M., and Gelencsér, A.: Light absorption properties of  
821 laboratory-generated tar ball particles, *Atmos. Chem. Phys.*, 16, 239-246, doi:10.5194/acp-16-239-2016, 2016.
- 822 Huang, K., Zhuang, G., Fu, J. S., Wang, Q., Liu, T., Zhang, R., Jiang, Y., Deng, C., Fu, Q., and Hsu, N.: Typical  
823 types and formation mechanisms of haze in an Eastern Asia megacity, Shanghai, *Atmos. Chem. Phys.*, 12,  
824 105-124, doi:10.5194/acp-12-105-2012, 2012.
- 825 Huang, R. J., Yang, L., Cao, J. J., Chen, Y., Chen, Q., Li, Y., Duan, J., Zhu, C., Dai, W., and Wang, K.: Brown  
826 carbon aerosol in Urban Xi'an, Northwest China: the composition and light absorption properties, *Environ. Sci.*  
827 *Technol.*, 52, 6825-6833, doi:10.1021/acs.est.8b02386, 2018.
- 828 IPCC. Climate Change 2013: the physical science basis. Contribution of working group I to the fifth assessment  
829 report of the intergovernmental panel on climate change. Cambridge, and New York, NY: Cambridge University  
830 Press, 2013.
- 831 Jacobson, M. Z.: Analysis of aerosol interactions with numerical techniques for solving coagulation, nucleation,  
832 condensation, dissolution, and reversible chemistry among multiple size distributions, *J. Geophys. Res. Atmos.*,  
833 107, D19, 4366, doi:10.1029/2001JD002044, 2002.
- 834 Jacobson, M. Z.: Effects of biomass burning on climate, accounting for heat and moisture fluxes, black and  
835 brown carbon, and cloud absorption effects, *J. Geophys. Res. Atmos.*, 119, 8980-9002,



- 836 [doi.org/10.1002/2014JD021861](https://doi.org/10.1002/2014JD021861), 2014.
- 837 Jimenez, J., Canagaratna, M., Donahue, N., Prevot, A., Zhang, Q., Kroll, J. H., DeCarlo, P. F., Allan, J. D., Coe,  
838 H., and Ng, N.: Evolution of organic aerosols in the atmosphere, *Science*, 326, 1525-1529, doi:  
839 10.1126/science.1180353, 2009.
- 840 Jo, D. S., Park, R. J., Lee, S., Kim, S. W., and Zhang, X.: A global simulation of brown carbon: implications for  
841 photochemistry and direct radiative effect, *Atmos. Chem. Phys.*, 16, 3413-3432, doi:10.5194/acp-16-3413-2016,  
842 2016.
- 843 Kanakidou, M., Seinfeld, J., Pandis, S., Barnes, I., Dentener, F., Facchini, M., Dingenen, R. V., Ervens, B.,  
844 Nenes, A., and Nielsen, C.: Organic aerosol and global climate modelling: a review, *Atmos. Chem. Phys.*, 5,  
845 1053-1123, doi: 1680-7324/acp/2005-5-1053, 2005.
- 846 Kang, E., Root, M., Toohey, D., and Brune, W.: Introducing the concept of potential aerosol mass (PAM), *Atmos.*  
847 *Chem. Phys.*, 7, 5727-5744, doi: 10.5194/acp-7-5727-2007, 2007.
- 848 Kim, H., Liu, S., Russell, L. M., and Paulson, S. E.: Dependence of real refractive indices on O:C, H:C and  
849 mass fragments of secondary organic aerosol generated from ozonolysis and photooxidation of limonene and  
850  $\alpha$ -pinene, *Aerosol Sci. Tech.*, 48, 498-507, doi: 10.1080/02786826.2014.893278, 2014.
- 851 Kroll, J. H., Donahue, N. M., Jimenez, J. L., Kessler, S. H., Canagaratna, M. R., Wilson, K. R., Altieri, K. E.,  
852 Mazzoleni, L. R., Wozniak, A. S., and Bluhm, H.: Carbon oxidation state as a metric for describing the  
853 chemistry of atmospheric organic aerosol, *Nat. Chem.*, 3, 133, doi: 10.1038/NCHEM.948, 2011.
- 854 Lack, D. A., Langridge, J. M., Bahreini, R., Cappa, C. D., Middlebrook, A. M., and Schwarz, J. P.: Brown  
855 carbon and internal mixing in biomass burning particles, *P. Natl. Acad. Sci. USA*, 109, 14802-14807,  
856 doi:10.1073/pnas.1206575109, 2012.
- 857 Lambe, A., Onasch, T., Massoli, P., Croasdale, D., Wright, J., Ahern, A., Williams, L., Worsnop, D., Brune, W.,  
858 and Davidovits, P.: Laboratory studies of the chemical composition and cloud condensation nuclei (CCN)  
859 activity of secondary organic aerosol (SOA) and oxidized primary organic aerosol (OPOA), *Atmos. Chem.*  
860 *Phys.*, 11, 8913-8928, doi: 10.5194/acp-11-8913-2011, 2011.
- 861 Lambe, A., Massoli, P., Zhang, X., Canagaratna, M., Nowak, J., Daube, C., Chao, Y., Nie, W., Onasch, T., and  
862 Jayne, J.: Controlled nitric oxide production via O (<sup>1</sup>D)+ N<sub>2</sub>O reactions for use in oxidation flow reactor studies,  
863 *Atmos. Meas. Tech.*, 10, 2283, doi: 10.5194/amt-10-2283-2017, 2017.
- 864 Laskin, A., Laskin, J., and Nizkorodov, S. A.: Chemistry of atmospheric brown carbon, *Chem. Rev.*, 115,  
865 4335-4382, doi: 10.1021/cr5006167, 2015.



- 866 Laskin, A., Smith, J. S., and Laskin, J.: Molecular characterization of nitrogen-containing organic compounds in  
867 biomass burning aerosols using high-resolution mass spectrometry, *Environ. Sci. Technol.*, 43, 3764-3771,  
868 doi:10.1021/es803456n, 2009.
- 869 Lee, H. J., Aiona, P. K., Laskin, A., Laskin, J., and Nizkorodov, S. A.: Effect of solar radiation on the optical  
870 properties and molecular composition of laboratory proxies of atmospheric brown carbon, *Environ. Sci.*  
871 *Technol.*, 48, 10217-10226, doi: 10.1021/es502515r, 2014.
- 872 Levinson, R., Akbari, H., and Berdahl, P.: Measuring solar reflectance-Part I: Defining a metric that accurately  
873 predicts solar heat gain, *Sol. Energy*, 84, 1717-1744, doi:10.1016/j.solener.2010.04.018, 2010.
- 874 Li, C., Ma, Z., Chen, J., Wang, X., Ye, X., Wang, L., Yang, X., Kan, H., Donaldson, D., and Mellouki, A.:  
875 Evolution of biomass burning smoke particles in the dark, *Atmos. Environ.*, 120, 244-252,  
876 doi:10.1016/j.atmosenv.2015.09.003, 2015.
- 877 Li, C., Hu, Y., Zhang, F., Chen, J., Ma, Z., Ye, X., Yang, X., Wang, L., Tang, X., and Zhang, R.: Multi-pollutant  
878 emissions from the burning of major agricultural residues in China and the related health-economic effects,  
879 *Atmos. Chem. Phys.*, 17, 4957-4988, doi: doi:10.5194/acp-17-4957-2017, 2017.
- 880 Li, Y., Huang, D., Cheung, H. Y., Lee, A., and Chan, C. K.: Aqueous-phase photochemical oxidation and direct  
881 photolysis of vanillin-a model compound of methoxy phenols from biomass burning, *Atmos. Chem. Phys.*, 14,  
882 2871-2885, doi:10.5194/acp-14-2871-2014, 2014.
- 883 Li, Y. J., Yeung, J. W., Leung, T. P., Lau, A. P., and Chan, C. K.: Characterization of organic particles from  
884 incense burning using an aerodyne high-resolution time-of-flight aerosol mass spectrometer, *Aerosol Sci. Tech.*,  
885 46, 654-665, doi:10.1080/02786826.2011.653017, 2012.
- 886 Lin, P., Liu, J., Shilling, J. E., Kathmann, S. M., Laskin, J., and Laskin, A.: Molecular characterization of brown  
887 carbon (BrC) chromophores in secondary organic aerosol generated from photo-oxidation of toluene, *Phys.*  
888 *Chem. Chem. Phys.*, 17, 23312-23325, doi:10.1039/C5CP02563J, 2015.
- 889 Lin, P., Aiona, P. K., Li, Y., Shiraiwa, M., Laskin, J., Nizkorodov, S. A., and Laskin, A.: Molecular  
890 characterization of brown carbon in biomass burning aerosol particles, *Environ. Sci. Technol.*, 50, 11815-11824,  
891 doi:10.1021/acs.est.6b03024, 2016.
- 892 Lin, P., Bluvshstein, N., Rudich, Y., Nizkorodov, S. A., Laskin, J., and Laskin, A.: Molecular Chemistry of  
893 Atmospheric Brown Carbon Inferred from a Nationwide Biomass Burning Event, *Environ. Sci. Technol.*, 51,  
894 11561-11570, doi:10.1021/acs.est.7b02276, 2017.





- 895 Liu, J., Bergin, M., Guo, H., King, L., Kotra, N., Edgerton, E., and Weber, R.: Size-resolved measurements of  
896 brown carbon in water and methanol extracts and estimates of their contribution to ambient fine-particle light  
897 absorption, *Atmos. Chem. Phys.*, 13, 12389-12404, doi:10.5194/acp-13-12389-2013, 2013.
- 898 Liu, J., Lin, P., Laskin, A., Laskin, J., Kathmann, S. M., Wise, M., Caylor, R., Imholt, F., Selimovic, V., and  
899 Shilling, J. E.: Optical properties and aging of light-absorbing secondary organic aerosol, *Atmos. Chem. Phys.*,  
900 16, 12815-12827, doi:10.5194/acp-16-12815-2016, 2016.
- 901 Lu, J. W., Flores, J. M., Lavi, A., Abo-Riziq, A., and Rudich, Y.: Changes in the optical properties of benzo[a]  
902 pyrene-coated aerosols upon heterogeneous reactions with NO<sub>2</sub> and NO<sub>3</sub>, *Phys. Chem. Chem. Phys.*, 13,  
903 6484-6492, doi:10.1039/C0CP02114H, 2011.
- 904 McDonald, J. D., Zielinska, B., Fujita, E. M., Sagebiel, J. C., Chow, J. C., and Watson, J. G.: Fine particle and  
905 gaseous emission rates from residential wood combustion, *Environ. Sci. Technol.*, 34, 2080-2091,  
906 doi:10.1021/es9909632, 2000.
- 907 Moise, T., Flores, J. M., and Rudich, Y.: Optical properties of secondary organic aerosols and their changes by  
908 chemical processes, *Chem. Rev.*, 115, 4400-4439, doi: 10.1021/cr5005259, 2015.
- 909 Miljevic, B., Hedayat, F., Stevanovic, S., Fairfull-Smith, K. E., Bottle, S., and Ristovski, Z.: To sonicate or not  
910 to sonicate PM filters: reactive oxygen species generation upon ultrasonic irradiation, *Aerosol Sci. Tech.*, 48,  
911 1276-1284, doi:10.1080/02786826.2014.981330, 2014.
- 912 Mutzel, A., Rodigast, M., Iinuma, Y., Böge, O., and Herrmann, H.: An improved method for the quantification  
913 of SOA bound peroxides, *Atmos. Environ.*, 67, 365-369, doi:10.1016/j.atmosenv.2012.11.012, 2013.
- 914 Ng, N., Chhabra, P., Chan, A., Surratt, J. D., Kroll, J., Kwan, A., McCabe, D., Wennberg, P., Sorooshian, A., and  
915 Murphy, S.: Effect of NO<sub>x</sub> level on secondary organic aerosol (SOA) formation from the photooxidation of  
916 terpenes, *Atmos. Chem. Phys.*, 7, 5159-5174, doi:10.5194/acp-7-5159-2007, 2007.
- 917 Ng, N., Canagaratna, M., Zhang, Q., Jimenez, J., Tian, J., Ulbrich, I., Kroll, J., Docherty, K., Chhabra, P., and  
918 Bahreini, R.: Organic aerosol components observed in Northern Hemispheric datasets from Aerosol Mass  
919 Spectrometry, *Atmos. Chem. Phys.*, 10, 4625-4641, doi:10.5194/acp-10-4625-2010, 2010.
- 920 Ng, N., Canagaratna, M., Jimenez, J., Chhabra, P., Seinfeld, J., and Worsnop, D.: Changes in organic aerosol  
921 composition with aging inferred from aerosol mass spectra, *Atmos. Chem. Phys.*, 11, 6465-6474,  
922 doi:10.5194/acp-11-6465-2011, 2011.



- 923 Park, R. J., Kim, M. J., Jeong, J. I., Youn, D., and Kim, S.: A contribution of brown carbon aerosol to the aerosol  
924 light absorption and its radiative forcing in East Asia, *Atmos. Environ.*, 44, 1414-1421,  
925 doi:10.1016/j.atmosenv.2010.01.042, 2010.
- 926 Passig, J., Schade, J., Oster, M., Fuchs, M., Ehlert, S., Jäger, C., Sklorz, M., and Zimmermann, R.: Aerosol mass  
927 spectrometer for simultaneous detection of polyaromatic hydrocarbons and inorganic components from  
928 individual particles, *Anal. Chem.*, 89, 6341-6345, doi:10.1021/acs.analchem.7b01207, 2017.
- 929 Peng, Z., Day, D., Stark, H., Li, R., Lee-Taylor, J., Palm, B., Brune, W., and Jimenez, J. L.: HO<sub>x</sub> radical  
930 chemistry in oxidation flow reactors with low-pressure mercury lamps systematically examined by modeling,  
931 *Atmos. Meas. Tech.*, 8, 4863-4890, doi:10.5194/amt-8-4863-2015, 2015.
- 932 Peng, Z., Day, D. A., Ortega, A. M., Palm, B. B., Hu, W., Stark, H., Li, R., Tsigaridis, K., Brune, W. H., and  
933 Jimenez, J. L.: Non-OH chemistry in oxidation flow reactors for the study of atmospheric chemistry  
934 systematically examined by modeling, *Atmos. Chem. Phys.*, 16, 4283-4305, doi:10.5194/acp-16-4283-2016,  
935 2016.
- 936 Peng, Z., and Jimenez, J. L.: Modeling of the chemistry in oxidation flow reactors with high initial NO, *Atmos.*  
937 *Chem. Phys.*, 17, 11991-12010, doi: 10.5194/acp-17-11991-2017, 2017.
- 938 Pettersson, A., Lovejoy, E. R., Brock, C. A., Brown, S. S., and Ravishankara, A.: Measurement of aerosol  
939 optical extinction at 532 nm with pulsed cavity ring down spectroscopy, *J. Aerosol Sci.*, 35, 995-1011,  
940 doi:10.1016/j.jaerosci.2004.02.008, 2004.
- 941 Phillips, S. M., and Smith, G. D.: Light absorption by charge transfer complexes in brown carbon aerosols,  
942 *Environ. Sci. Technol. Lett.*, 1, 382-386, doi:10.1021/ez500263j, 2014.
- 943 Pósfai, M., Gelencsér, A., Simonics, R., Arató, K., Li, J., Hobbs, P. V., and Buseck, P. R.: Atmospheric tar balls:  
944 Particles from biomass and biofuel burning, *J. Geophys. Res. Atmos.*, 109, D06213, doi:10.1029/2003JD004169,  
945 2004.
- 946 Reid, J. S., Eck, T. F., Christopher, S. A., Koppmann, R., Dubovik, O., Eleuterio, D., Holben, B. N., Reid, E. A.,  
947 and Zhang, J.: A review of biomass burning emissions part III: intensive optical properties of biomass burning  
948 particles, *Atmos. Chem. Phys.*, 5, 827-849, doi: 10.5194/acp-5-827-2005, 2005.
- 949 Rettner, C. T., and Brophy, J. H.: Resonance enhanced laser ionisation mass spectrometry of four aromatic  
950 molecules, *Chem. Phys.*, 56, 53-61, doi:10.1016/0301-0104(81)85099-9, 1981.



- 951 Rollins, A. W., Browne, E. C., Min, K. E., Pusede, S. E., Wooldridge, P. J., Gentner, D. R., Goldstein, A. H., Liu,  
952 S., Day, D. A., and Russell, L. M.: Evidence for NO<sub>x</sub> control over nighttime SOA formation, *Science*, 337,  
953 1210-1212, doi:10.1126/science.1221520, 2012.
- 954 Rudich, Y., Donahue, N. M., and Mentel, T. F.: Aging of organic aerosol: Bridging the gap between laboratory  
955 and field studies, *Annu. Rev. Phys. Chem.*, 58, 321-352, doi:10.1146/annurev.physchem.58.032806.104432,  
956 2007.
- 957 Russell, P., Bergstrom, R., Shinozuka, Y., Clarke, A., DeCarlo, P., Jimenez, J., Livingston, J., Redemann, J.,  
958 Dubovik, O., and Strawa, A.: Absorption Ångström Exponent in AERONET and related data as an indicator of  
959 aerosol composition, *Atmos. Chem. Phys.*, 10, 1155-1169, doi: 10.5194/acp-10-1155-2010, 2010.
- 960 Samburova, V., Connolly, J., Gyawali, M., Yatavelli, R. L., Watts, A. C., Chakrabarty, R. K., Zielinska, B.,  
961 Moosmüller, H., and Khlystov, A.: Polycyclic aromatic hydrocarbons in biomass-burning emissions and their  
962 contribution to light absorption and aerosol toxicity, *Sci. Total Environ.*, 568, 391-401,  
963 doi:10.1016/j.scitotenv.2016.06.026, 2016.
- 964 Schauer, J. J., Kleeman, M. J., Cass, G. R., and Simoneit, B. R.: Measurement of emissions from air pollution  
965 sources. 3. C1-C29 organic compounds from fireplace combustion of wood, *Environ. Sci. Technol.*, 35,  
966 1716-1728, doi:10.1021/es001331e, 2001.
- 967 Sedlacek III, A. J., Buseck, P. R., Adachi, K., Onasch, T. B., Springston, S. R., and Kleinman, L.: Formation and  
968 evolution of Tar Balls from Northwestern US wildfires, *Atmos. Chem. Phys.*, 18, 11289-11301,  
969 doi:10.5194/acp-18-11289-2018, 2018.
- 970 Seinfeld, J. H., and Pandis, S. N.: *Atmospheric chemistry and physics: from air pollution to climate change*, 3rd  
971 edition, John Wiley & Sons, Inc., Hoboken, New Jersey, USA, 2016.
- 972 Shamjad, P. M., Satish, R. V., Thamban, N. M., Rastogi, N., and Tripathi, S.: Absorbing refractive index and  
973 direct radiative forcing of atmospheric Brown Carbon over Gangetic Plain, *ACS Earth Space Chem.*, 2, 31-37,  
974 doi:10.1021/acsearthspacechem.7b00074, 2018.
- 975 Shen, G., Tao, S., Wei, S., Zhang, Y., Wang, R., Wang, B., Li, W., Shen, H., Huang, Y., and Yang, Y.: Retene  
976 emission from residential solid fuels in China and evaluation of retene as a unique marker for soft wood  
977 combustion, *Environ. Sci. Technol.*, 46, 4666-4672, doi:10.1021/es300144m, 2012.
- 978 Shen, H., Huang, Y., Wang, R., Zhu, D., Li, W., Shen, G., Wang, B., Zhang, Y., Chen, Y., and Lu, Y.: Global  
979 atmospheric emissions of polycyclic aromatic hydrocarbons from 1960 to 2008 and future predictions, *Environ.*  
980 *Sci. Technol.*, 47, 6415-6424, doi:10.1021/es400857z, 2013.



- 981 Shrivastava, M., Cappa, C. D., Fan, J., Goldstein, A. H., Guenther, A. B., Jimenez, J. L., Kuang, C., Laskin, A.,  
982 Martin, S. T., and Ng, N. L.: Recent advances in understanding secondary organic aerosol: Implications for  
983 global climate forcing, *Rev. Geophys.*, 55, 509-559, doi: 10.1002/2016RG000540, 2017.
- 984 Sigsgaard, T., Forsberg, B., Annesi-Maesano, I., Blomberg, A., Bølling, A., Boman, C., Bønløkke, J., Brauer, M.,  
985 Bruce, N., and Héroux, M. E.: Health impacts of anthropogenic biomass burning in the developed world, *Eur.*  
986 *Respir. J.*, 46, 1577-1588, doi:10.1183/13993003.01865-2014, 2015.
- 987 Sumlin, B. J., Pandey, A., Walker, M. J., Pattison, R. S., Williams, B. J., and Chakrabarty, R. K.: Atmospheric  
988 Photooxidation Diminishes Light Absorption by Primary Brown Carbon Aerosol from Biomass Burning,  
989 *Environ. Sci. Technol. Lett.*, 4, 540-545, doi:10.1021/acs.estlett.7b00393, 2017.
- 990 Sumlin, B. J., Oxford, C. R., Seo, B., Pattison, R. R., Williams, B. J., and Chakrabarty, R. K.: Density and  
991 homogeneous internal composition of primary brown carbon aerosol, *Environ. Sci. Technol.*, 52, 3982-3989, doi:  
992 10.1021/acs.est.8b00093, 2018.
- 993 Tavakoli, F., and Olfert, J.: An instrument for the classification of aerosols by particle relaxation time:  
994 theoretical models of the aerodynamic aerosol classifier, *Aerosol Sci. Tech.*, 47, 916-926,  
995 doi:10.1080/02786826.2013.802761, 2013.
- 996 Tavakoli, F., and Olfert, J. S.: Determination of particle mass, effective density, mass-mobility exponent, and  
997 dynamic shape factor using an aerodynamic aerosol classifier and a differential mobility analyzer in tandem, *J.*  
998 *Aerosol Sci.*, 75, 35-42, doi:10.1016/j.jaerosci.2014.04.010, 2014.
- 999 Tóth, A., Hoffer, A., Nyirő-Kósa, I., Pósfai, M., and Gelencsér, A.: Atmospheric tar balls: aged primary droplets  
1000 from biomass burning?, *Atmos. Chem. Phys.*, 14, 6669-6675, doi:10.5194/acp-14-6669-2014, 2014.
- 1001 Washenfelder, R., Attwood, A., Brock, C., Guo, H., Xu, L., Weber, R., Ng, N., Allen, H., Ayres, B., and  
1002 Baumann, K.: Biomass burning dominates brown carbon absorption in the rural southeastern United States,  
1003 *Geophys. Res. Lett.*, 42, 653-664, doi:10.1002/2014GL062444, 2015.
- 1004 Washenfelder, R., Flores, J., Brock, C., Brown, S., and Rudich, Y.: Broadband measurements of aerosol  
1005 extinction in the ultraviolet spectral region, *Atmos. Meas. Tech.*, 6, 861-877, doi:10.5194/amt-6-861-2013, 2013.
- 1006 Wei, C., Bandowe, B. A. M., Han, Y., Cao, J., Zhan, C., and Wilcke, W.: Polycyclic aromatic hydrocarbons  
1007 (PAHs) and their derivatives (alkyl-PAHs, oxygenated-PAHs, nitrated-PAHs and azaarenes) in urban road dusts  
1008 from Xi'an, Central China, *Chemosphere*, 134, 512-520, doi:10.1016/j.chemosphere.2014.11.052, 2015.



- 1009 Weimer, S., Alfarra, M., Schreiber, D., Mohr, M., Prévôt, A., and Baltensperger, U.: Organic aerosol mass  
1010 spectral signatures from wood-burning emissions: Influence of burning conditions and wood type, *J. Geophys.*  
1011 *Res. Atmos.*, 113, doi:10.1029/2007JD009309, 2008.
- 1012 Wong, J. P., Zhou, S., and Abbatt, J. P.: Changes in secondary organic aerosol composition and mass due to  
1013 photolysis: relative humidity dependence, *J. Phys. Chem. A*, 119, 4309-4316, doi: 10.1021/jp506898c, 2014.
- 1014 Xie, M., Hays, M. D., and Holder, A. L.: Light-absorbing organic carbon from prescribed and laboratory  
1015 biomass burning and gasoline vehicle emissions, *Scientific Reports*, 7, 7318, doi:10.1038/s41598-017-06981-8,  
1016 2017.
- 1017 Yee, L., Kautzman, K., Loza, C., Schilling, K., Coggon, M., Chhabra, P., Chan, M., Chan, A., Hersey, S., and  
1018 Crouse, J.: Secondary organic aerosol formation from biomass burning intermediates: phenol and  
1019 methoxyphenols, *Atmos. Chem. Phys.*, 13, 8019-8043, doi:10.5194/acp-13-8019-2013, 2013.
- 1020 Yu, L., Smith, J., Laskin, A., Anastasio, C., Laskin, J., and Zhang, Q.: Chemical characterization of SOA formed  
1021 from aqueous-phase reactions of phenols with the triplet excited state of carbonyl and hydroxyl radical, *Atmos.*  
1022 *Chem. Phys.*, 14, 13801-13816, doi:10.5194/acp-14-13801-2014, 2014.
- 1023 Zhang, H., and Ying, Q.: Secondary organic aerosol from polycyclic aromatic hydrocarbons in Southeast Texas,  
1024 *Atmos. Environ.*, 55, 279-287, doi:10.1016/j.atmosenv.2012.03.043, 2012.
- 1025 Zhang, X., and Seinfeld, J.: A functional group oxidation model (FGOM) for SOA formation and aging, *Atmos.*  
1026 *Chem. Phys.*, 13, 5907-5926, doi: 10.5194/acp-14-13801-2014, 2013.
- 1027 Zhong, M., and Jang, M.: Dynamic light absorption of biomass-burning organic carbon photochemically aged  
1028 under natural sunlight, *Atmos. Chem. Phys.*, 14, 1517-1525, doi: 10.5194/acp-14-1517-2014, 2014.
- 1029 Zhou, S., Collier, S., Jaffe, D. A., Briggs, N. L., Hee, J., Sedlacek III, A. J., Kleinman, L., Onasch, T. B., and  
1030 Zhang, Q.: Regional influence of wildfires on aerosol chemistry in the western US and insights into atmospheric  
1031 aging of biomass burning organic aerosol, *Atmos. Chem. Phys.*, 17, 2477-2493, doi: 10.5194/acp-17-2477-2017,  
1032 2017.
- 1033

1034 **Caption of Table and Figure**1035 **Table 1.** Summary of experimental conditions for tar balls photochemical oxidation1036 **Table 2.** Comparison of tar ball particle optical parameters with reference values of BBOA (mean ± standard  
1037 deviation)1038 **Figure 1.** Experimental setup for laboratory generation and aging of tar ball aerosol: including generation setup,  
1039 OFR photochemical aging, gaseous-particulate chemical monitoring, particle size distribution and optical  
1040 properties measurements.1041 **Figure 2.** High-resolution AMS mass spectra of fresh polar and nonpolar tar ball particles. Four ion groups are  
1042 grouped for clarity as:  $C_xH_y^+$  (green),  $C_xH_yO^+$  (purple),  $C_xH_yO_z^+$  ( $z > 1$ ) (violet),  $C_xH_yO_iN_p^+$  ( $i \geq 0$ ,  $p \geq 1$ ) (light  
1043 blue). The mass fractions of the four fragment groups are presented by pie-charts.1044 **Figure 3.** LD-REMPI mass spectra of exemplary single tar ball particles, some feature peaks were identified  
1045 and labeled. a) Nonpolar tar ball spectra shows predominantly alkyl-substituted and unsubstituted PAHs. b)  
1046 Polar tar ball spectra reveals many oxidized aromatics, e.g., methoxy-phenol, benzenediol. Note the softwood  
1047 combustion marker retene at  $m/z=234$ , its characteristic fragments ( $m/z=203, 204, 205, 219$ ) and possible retene  
1048 derivatives ( $m/z=248, 250$ ).1049 **Figure 4.** Wavelength-dependent RI and SSA for tar ball particles generated from polar, nonpolar and mixture of  
1050 the two phases tarry solutions (only retrieval for mixture of 1:1 in vol. is shown for clarity, optical results for the  
1051 rest two mixtures can be found in supporting materials). The shaded areas indicate the upper and lower limits of  
1052 the imaginary part calculated from UV-Vis spectra of methanol extracts from the corresponding tar ball particles  
1053 samples: a) real part, b) imaginary part, and c) SSA calculated for 150 nm particles. Overplayed in green symbol  
1054 are previous measurements of biomass burning from the literature.1055 **Figure 5.** Evolution of the retrieved wavelength-dependent complex RI and SSA as a function of O:C ratio for  
1056 tar ball particles upon OH photochemical oxidation: a) real part, b) imaginary part, and c) SSA calculated for  
1057 150 nm particles. The color scale shows the span in the RI for the wavelengths measured from 365 to 425 nm.  
1058 For clarity, error bars for O:C ratio ( $\pm 0.01$ ), RI ( $\pm 0.007$  for real part, and  $\pm 0.003$  for imaginary part on average),  
1059 and SSA ( $\pm 0.006$ ) are not shown. Two dashed lines trace the RI and SSA at 375 nm (purple) and 405 nm (green).  
1060 O<sub>0.7</sub>~O<sub>6.7</sub> represent equivalent atmospheric photochemical oxidation for 0.7 and up to 6.7 days.1061 **Figure 6.** Dynamic changes for the chemical characteristics of tar ball particle under NO<sub>x</sub>-free OH  
1062 photochemical oxidation: a) OM/OC, H:C ratio, particle density, and average carbon oxidation state ( $\overline{OSC}$ )



1063 changes as a function of O:C ratio; b) mass spectra evolution with oxidation times in term of  $C_xH_y^+$ ,  $C_xH_yO^+$ ,  
1064  $C_xH_yO_z^+$ , and  $C_xH_yO_iN_p^+$  fragment groups.

1065 **Figure 7.** Comparison of  $f_{44}$  and  $f_{43}$  values from ambient data sets (Ng. et al., 2010) and values from ambient  
1066 biomass burning organic aerosol.

1067 **Figure 8.** Dynamic changes for chemical characteristics of tar ball aerosols under  $NO_x$ -dependent OH  
1068 photochemical oxidation: a) OM/OC, O:C, H:C, and particle density changes; b) mass spectra changes with  
1069 different oxidation conditions in term of  $C_xH_y^+$ ,  $C_xH_yO^+$ ,  $C_xH_yO_z^+$ , and  $C_xH_yO_zN_p^+$  fragment groups.  $C_xH_yO_zN_p^+$   
1070 include all nitrogen-containing fragments, (e.g.,  $C_xH_yON^+$ ,  $C_xH_yO_zNi^+$ ,  $C_xH_yN^+$ , etc.),  $NO_y^+$  include  $NO^+$  and  
1071  $NO_2^+$ . O\_3.9 represents 3.9 days equivalent atmospheric photochemical aging in absence of  $NO_x$ , N\_0.5 and  
1072 N\_2.0 indicate photochemical oxidation with 0.5 and 2.0 vol.%  $N_2O$  addition at ~4.0 days atmospheric  
1073 oxidation.

1074 **Figure 9.** Changes of retrieved spectra-dependent RI as a function of O:C ratio for tar ball particles upon  
1075  $NO_x$ -dependent photochemical oxidation: a) real part, b) imaginary part, and c) SSA calculated from 150 nm  
1076 particles. For clarity, error bars for O:C ratio ( $\pm 0.01$ ), RI ( $\pm 0.006$  for real part, and  $\pm 0.003$  for imaginary part on  
1077 average), and SSA ( $\pm 0.007$ ) are not shown. O\_3.9 represents 3.9 days equivalent atmospheric photochemical  
1078 aging in absence of  $NO_x$ , N\_0.5 and N\_2.0 indicate photochemical oxidation with 0.5 and 2.0 vol.%  $N_2O$   
1079 addition at ~4.0 days atmospheric oxidation.

1080 **Figure 10.** Size-resolved light extinction and absorption efficiency ratio of  $NO_x$ -dependent photooxidized tar  
1081 balls compared to the fresh tar ball particles: a) and c) extinction ratios at 375 and 405 nm, b) and d) absorption  
1082 ratios at 375 and 405 nm. O\_3.9 represents 3.9 days equivalent atmospheric photochemical aging in absence of  
1083  $NO_x$ , N\_0.5 and N\_2.0 indicate photochemical oxidation with 0.5 and 2.0 vol.%  $N_2O$  addition at ~4.0 days  
1084 atmospheric oxidation.

1085 **Figure 11.** Calculated size-resolved simple radiative forcing (SRF,  $W g^{-1}$ ) by tar ball aerosols, integrated over  
1086 365~425 nm incident solar irradiation for fresh and  $NO_x$ -dependent photooxidized tar balls: a) ground-based  
1087 radiative forcing, b) snow-based radiative forcing.

1088 **Table 1.** Summary of experimental conditions for tar ball particles photochemical oxidation

Experiment	O <sub>3</sub> (ppm)	N <sub>2</sub> O mixing ratio	Endpoint NO <sub>x</sub> (ppb)	RH (%)	water mixing ratio	Exposure	
						OH radical (molecules cm <sup>-3</sup> s)	photon flux (photons cm <sup>-2</sup> )
P1	—	—	—	38.90	0.0126	—	7.47E+15
P2	—	—	—	39.70	0.0128	—	4.83E+16
P3	—	—	—	40.50	0.0130	—	1.00E+17
O_0.7	24.46	—	—	37.29	0.0120	8.68E+10	1.56E+15
O_1.7	24.76	—	—	37.66	0.0122	2.23E+11	7.47E+15
O_3.9	24.63	—	—	35.58	0.0115	5.11E+11	4.83E+16
O_6.7	25.31	—	—	35.67	0.0116	8.65E+11	5.17E+16
N_0.5	24.18	0.005	96.1	36.60	0.0118	5.37E+11	5.92E+16
N_2.0	28.21	0.020	528.3	35.90	0.0116	4.85E+11	1.00E+17

1089 Note: P1~P3 mean photolysis test, O\_0.7~O\_6.7 correspond to photochemical oxidation experiment from equivalent 0.7 day to 6.7 days  
1090 ageing, and N\_0.5 and N\_2.0 indicate photochemical oxidation with N<sub>2</sub>O addition at 0.5 vol.% and 2 vol.% mixing ratios (standard  
1091 deviation for the parameters were not given in above table)





1092

**Table 2.** Compare of tar ball particle optical properties with reference values of BBOA (mean  $\pm$  standard deviation)

BrC	Complex Refractive index			$\hat{A}_{abs}$	$\hat{A}_{abs\_UVVIS}$	$\hat{A}_{ext}$	Reference
	Average	375nm	405nm				
	Nonpolar	(1.661 $\pm$ 0.008 $\pm$ (0.020 $\pm$ 0.004))i	(1.671 $\pm$ 0.003 $\pm$ (0.025 $\pm$ 0.003))i				
Mixture (2:1 in vol.)	(1.670 $\pm$ 0.010 $\pm$ (0.017 $\pm$ 0.004))i	(1.682 $\pm$ 0.008 $\pm$ (0.021 $\pm$ 0.002))i	(1.668 $\pm$ 0.007 $\pm$ (0.013 $\pm$ 0.001))i	6.79 $\pm$ 0.91	7.08	4.01 $\pm$ 0.09	This work
Mixture (1:1 in vol.)	(1.694 $\pm$ 0.011 $\pm$ (0.013 $\pm$ 0.003))i	(1.703 $\pm$ 0.015 $\pm$ (0.017 $\pm$ 0.001))i	(1.689 $\pm$ 0.011 $\pm$ (0.009 $\pm$ 0.002))i	6.16 $\pm$ 0.54	7.38	3.73 $\pm$ 0.23	
Mixture (1:2 in vol.)	(1.672 $\pm$ 0.010 $\pm$ (0.011 $\pm$ 0.004))i	(1.683 $\pm$ 0.005 $\pm$ (0.018 $\pm$ 0.002))i	(1.667 $\pm$ 0.003 $\pm$ (0.006 $\pm$ 0.003))i	6.66 $\pm$ 0.63	7.24	4.06 $\pm$ 0.11	
Polar	(1.635 $\pm$ 0.009 $\pm$ (0.003 $\pm$ 0.003))i	(1.647 $\pm$ 0.003 $\pm$ (0.005 $\pm$ 0.001))i	(1.635 $\pm$ 0.004 $\pm$ (0.004 $\pm$ 0.003))i	6.72 $\pm$ 2.28 <sup>a</sup>	7.83	3.93 $\pm$ 0.06	Sumlin et al., 2017, 2018
BBOA	1.590 $\pm$ 0.029 $\pm$ (0.0375nm, 1.570 $\pm$ 0.010 $\pm$ (0.045nm (IPN)			6.4-7.4			Flowers et al., 2010
BBOA		1.590 $\pm$ 0.017 $\pm$ (0.05nm (IPN)					Lack et al., 2012
BBOA		k: 0.009 $\pm$ (0.04nm (CRDS-PAS)					Chakrabarty et al., 2010
Tar ball		1.78 $\pm$ 0.015i, 1.83 $\pm$ 0.0086 $\pm$ (0.05nm (IPN)		4.2-6.4			Hand et al., 2005
Tar ball		1.56 $\pm$ 0.021 $\pm$ (0.05nm (CRDS-UVVIS)					Adler et al., 2011
BBOA	1.53 $\pm$ 0.07i (WELAS, open fire), 1.54 $\pm$ 0.04i (WELAS, smoldering)						Blivisstein et al., 2017
BBOA		1.64 $\pm$ 0.03i $\pm$ (0.05nm (BBCES-Neph)		4-6 <sup>b</sup>		2-3 <sup>b</sup>	Hoffler et al., 2006
BBOA_HULIS		1.653 $\pm$ 0.002i, 1.685 $\pm$ 0.002 $\pm$ (0.532nm(Nep-PAS)			6-7		Dinar et al., 2008
BBOA_HULIS		1.616 $\pm$ 0.023 $\pm$ (0.390nm(CRDS)					Washenfelder et al., 2015
BBOA		1.550 $\pm$ 0.033 $\pm$ (0.365nm (BBCES)					Chen and Bond, 2010
BBOA					6.9-11.4 <sup>c</sup>		Xie et al., 2017
Ambient SOA					5.3-8.1 <sup>c</sup>		Huang et al., 2018
Ambient SOA		k: 0.046 $\pm$ (0.365nm, 0.039 $\pm$ (0.05nm, 0.036 $\pm$ (0.420nm (LWCC)					Shamjad et al., 2018

1093

Note:  $\hat{A}_{abs}$  and  $\hat{A}_{ext}$  were calculated from tar ball particle with median diameter of 150 nm in this study

1094

<sup>a</sup> regressed over wavelength range of 365–400 nm, no absorption detected over 410 nm using BBCES system

1095

<sup>b</sup> regressed over wavelength range of 300–650 nm for bulk fire plume emissions

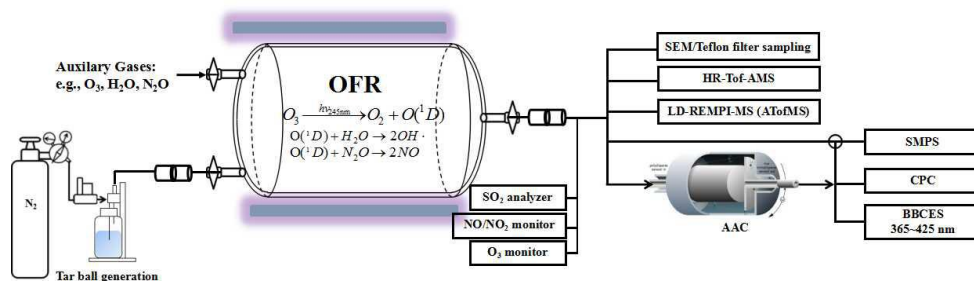
1096

<sup>c</sup>  $\hat{A}_{abs\_UVVIS}$  of methanol extracts over whole range from 300/560–600 nm

1097

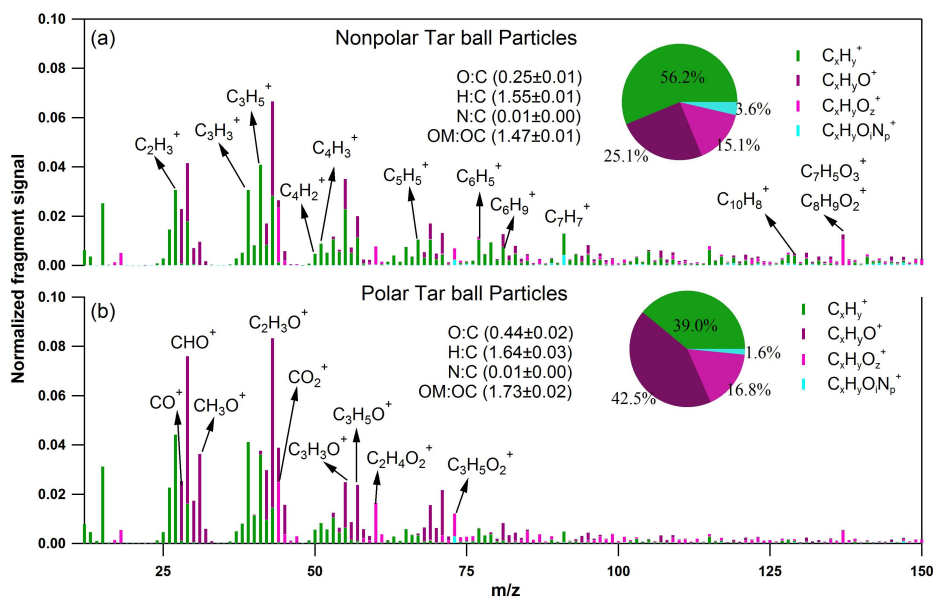
Instrument: IPN(integrated photoacoustic nephelometer), CRDS (cavity ring-down spectrometer), PAS (photoacoustic absorption spectrometer), WELAS (white light optical particle counter), LWCC (a liquid waveguide capillary cell)

1098



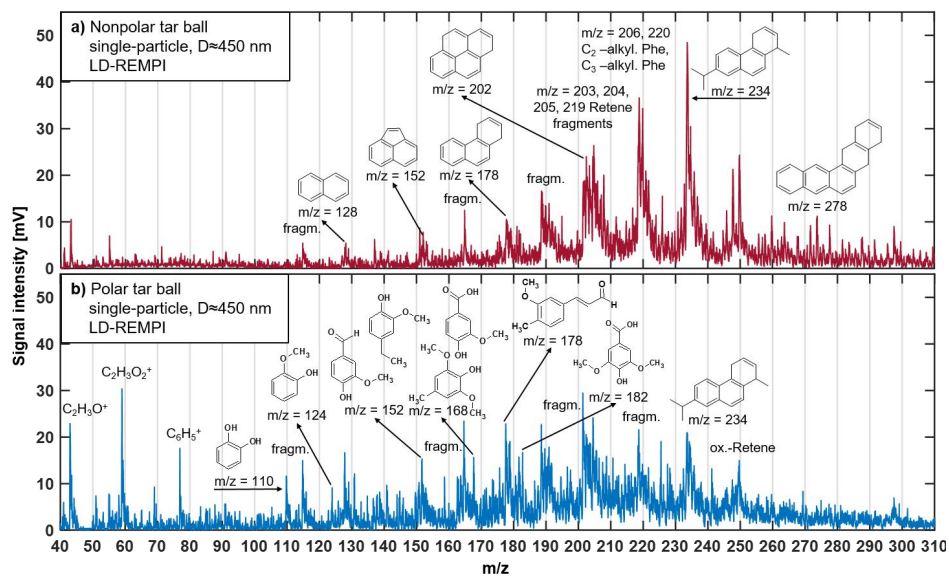
1099

1100 **Figure 1.** Experimental setup for laboratory generation and aging of tar ball aerosol: including generation setup, OFR  
 1101 photochemical aging, gaseous-particulate chemical monitoring, particle size distribution and optical properties  
 1102 measurements.



1103

1104 **Figure 2.** High-resolution AMS mass spectra of fresh polar and nonpolar tar ball particles. Four ion groups are grouped for  
 1105 clarity as:  $C_xH_y^+$  (green),  $C_xH_yO^+$  (purple),  $C_xH_yO_z^+$  ( $z > 1$ ) (violet),  $C_xH_yON_p^+$  ( $i \geq 0, p \geq 1$ ) (light blue). The mass fractions of  
 1106 the four fragment groups are presented by pie-charts.

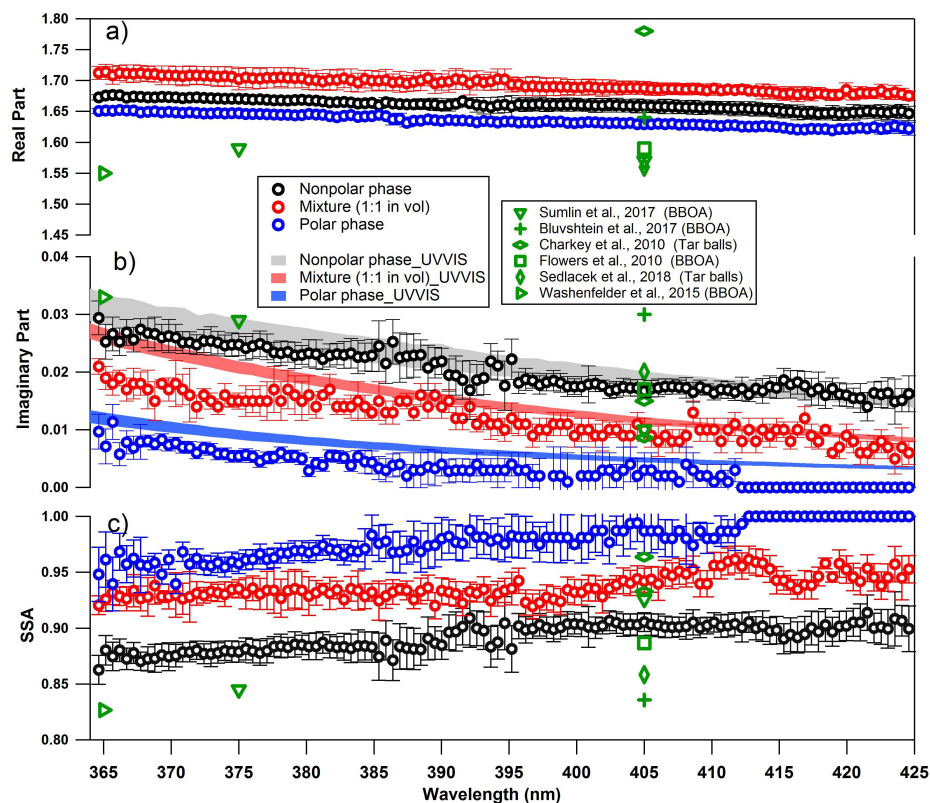


1107

1108 **Figure 3.** LD-REMPI mass spectra of exemplary single tar ball particles, some feature peaks were identified and labeled. a)

1109 Nonpolar tar ball spectra shows predominantly alkyl-substituted and unsubstituted PAHs. b) Polar tar ball spectra reveals

1110 many oxidized aromatics, e.g., methoxy-phenol, benzenediol. Note the softwood combustion marker retene at  $m/z=234$ , its1111 characteristic fragments ( $m/z=203, 204, 205, 219$ ) and possible retene derivatives ( $m/z=248, 250$ ).



1112

1113 **Figure 4.** Wavelength-dependent RI and SSA for tar ball particles generated from polar, nonpolar and mixture of the two

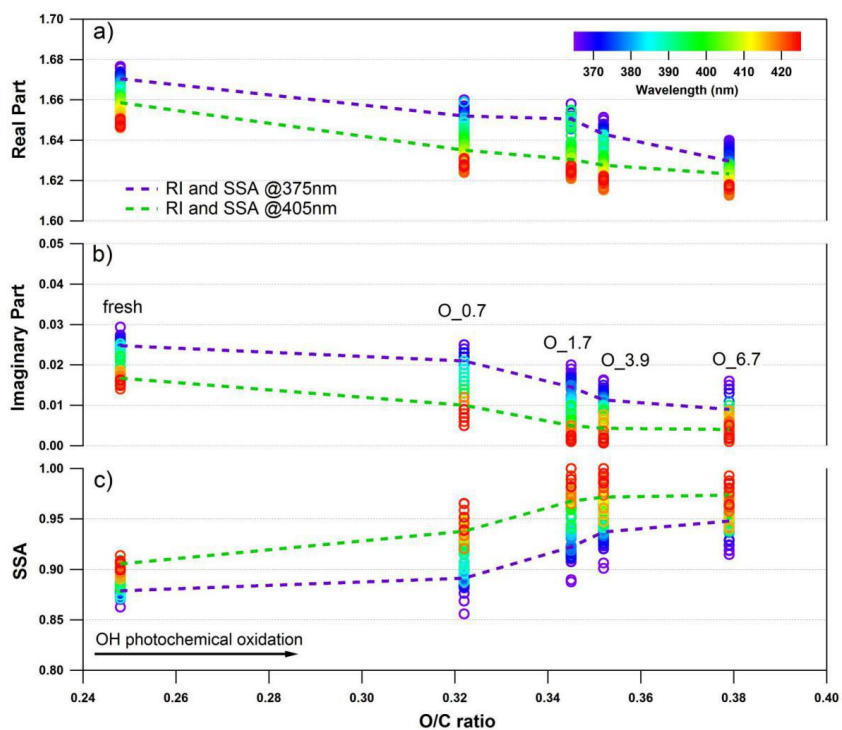
1114 phases tarry solutions (only retrieval for mixture of 1:1 in vol. is shown for clarity, optical results for the rest two mixtures

1115 can be found in supporting materials). The shaded areas indicate the upper and lower limits of the imaginary part calculated

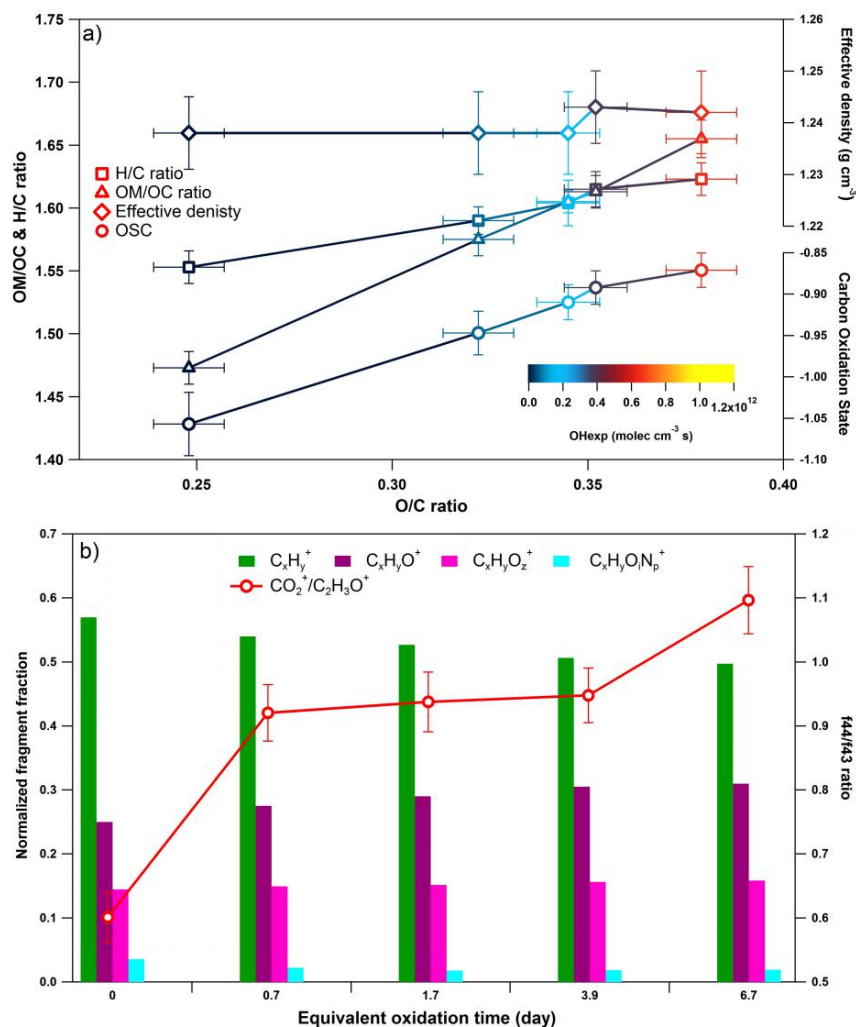
1116 from UV-VIS spectra of methanol extracts from the corresponding tar ball particles samples: a) real part, b) imaginary part,

1117 and c) SSA calculated for 150 nm particles. Overplayed in green symbol are previous measurements of biomass burning

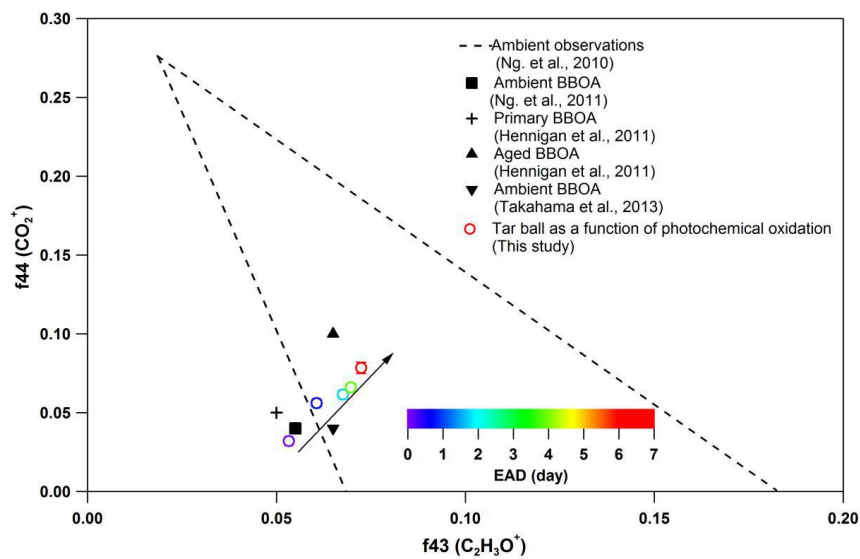
1118 from the literature.



1119 **Figure 5.** Evolution of the retrieved wavelength-dependent complex RI and SSA as a function of O:C ratio for tar ball  
1120 particles upon OH photochemical oxidation: a) real part, b) imaginary part, and c) SSA calculated for 150 nm particles. The  
1121 color scale shows the span in the RI for the wavelengths measured from 365 to 425 nm. For clarity, error bars for O:C ratio  
1122 ( $\pm 0.01$ ), RI ( $\pm 0.007$  for real part, and  $\pm 0.003$  for imaginary part on average), and SSA ( $\pm 0.006$ ) are not shown. Two dashed  
1123 lines trace the RI and SSA at 375 nm (purple) and 405 nm (green). O<sub>0.7</sub>-O<sub>6.7</sub> represent equivalent atmospheric  
1124 photochemical oxidation for 0.7 and up to 6.7 days.

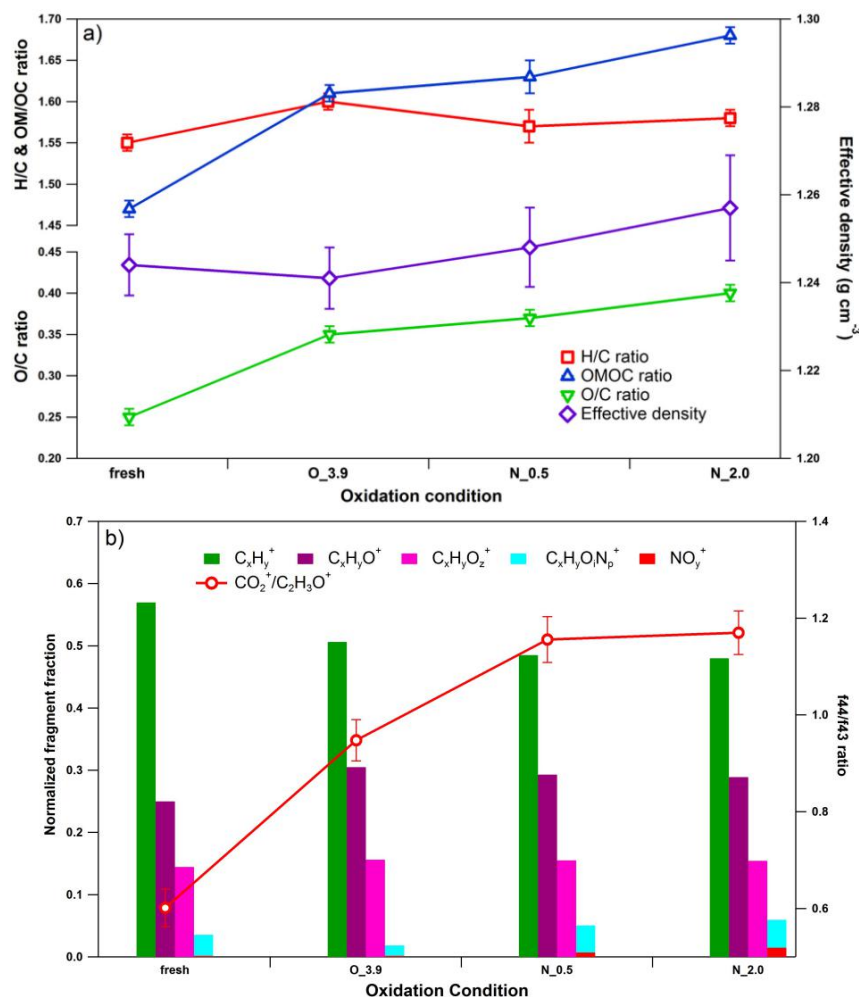


1125 **Figure 6.** Dynamic changes for the chemical characteristics of tar ball particle under NO<sub>x</sub>-free OH photochemical oxidation:  
 1126 a) OM/OC, H:C ratio, particle density, and average carbon oxidation state ( $\overline{OSc}$ ) changes as a function of O:C ratio; b) mass  
 1127 spectra evolution with oxidation times in term of C<sub>x</sub>H<sub>y</sub><sup>+</sup>, C<sub>x</sub>H<sub>y</sub>O<sup>+</sup>, C<sub>x</sub>H<sub>y</sub>O<sub>2</sub><sup>+</sup>, and C<sub>x</sub>H<sub>y</sub>O<sub>i</sub>N<sub>p</sub><sup>+</sup> fragment groups.

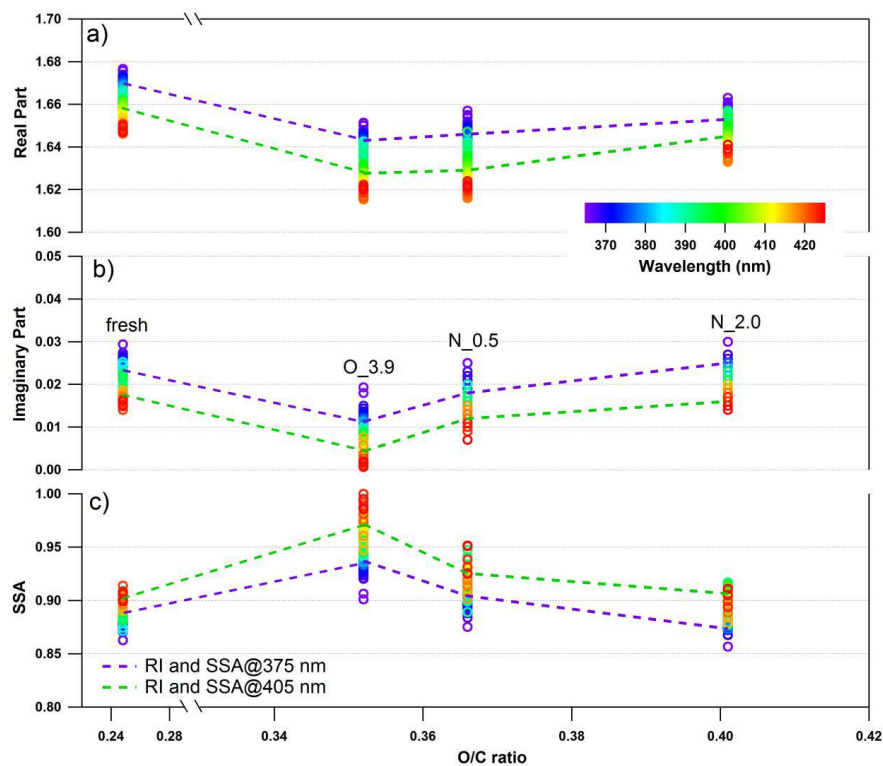


1128 **Figure 7.** Comparison of f44 and f43 values from ambient data sets (Ng. et al., 2010) and values from ambient biomass  
1129 burning organic aerosol. The hollow circles present tar ball result in this work, and color legend indicate equivalent  
1130 atmospheric oxidation days, black arrow more clearly shows the extent of NO<sub>x</sub>-free photochemical oxidation in this study.



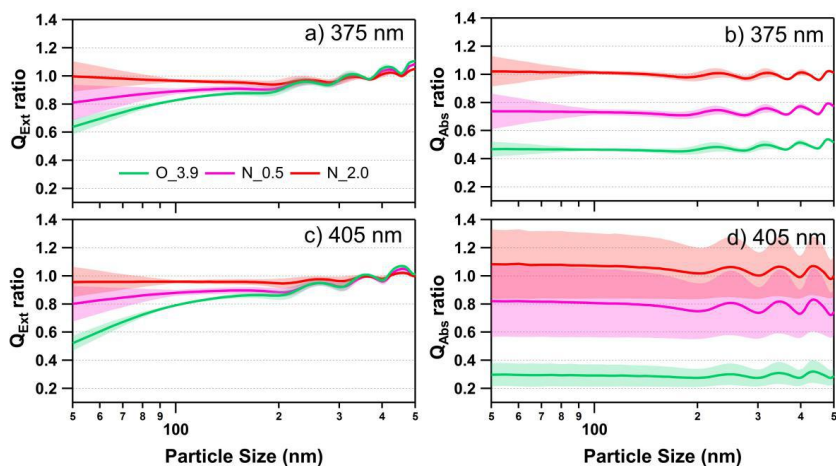


1131 **Figure 8.** Dynamic changes for chemical characteristics of tar ball aerosols under  $NO_x$ -dependent OH photochemical  
 1132 oxidation: a) OM/OC, O:C, H:C, and particle density changes; b) mass spectra changes with different oxidation conditions in  
 1133 term of  $C_xH_y^+$ ,  $C_xH_yO^+$ ,  $C_xH_yO_2^+$ , and  $C_xH_yO_2N_p^+$  fragment groups.  $C_xH_yO_2N_p^+$  include all nitrogen-containing fragments,  
 1134 (e.g.,  $C_xH_yON^+$ ,  $C_xH_yO_2N^+$ ,  $C_xH_yN^+$ , etc.),  $NO_y^+$  include  $NO^+$  and  $NO_2^+$ . O\_3.9 represents 3.9 days equivalent atmospheric  
 1135 photochemical aging in absence of  $NO_x$ , N\_0.5 and N\_2.0 indicate photochemical oxidation with 0.5 and 2.0 vol.%  $N_2O$   
 1136 addition at ~4.0 days atmospheric oxidation.



1137

1138 **Figure 9.** Changes of retrieved spectra-dependent RI as a function of O:C ratio for tar ball particles upon NO<sub>x</sub>-dependent  
 1139 photochemical oxidation: a) real part, b) imaginary part, and c) SSA calculated from 150 nm particles. For clarity, error bars  
 1140 for O:C ratio ( $\pm 0.01$ ), RI ( $\pm 0.006$  for real part, and  $\pm 0.003$  for imaginary part on average), and SSA ( $\pm 0.007$ ) are not  
 1141 shown. O\_3.9 represents 3.9 days equivalent atmospheric photochemical aging in absence of NO<sub>x</sub>, N\_0.5 and N\_2.0 indicate  
 1142 photochemical oxidation with 0.5 and 2.0 vol.% N<sub>2</sub>O addition at  $\sim 4.0$  days atmospheric oxidation.



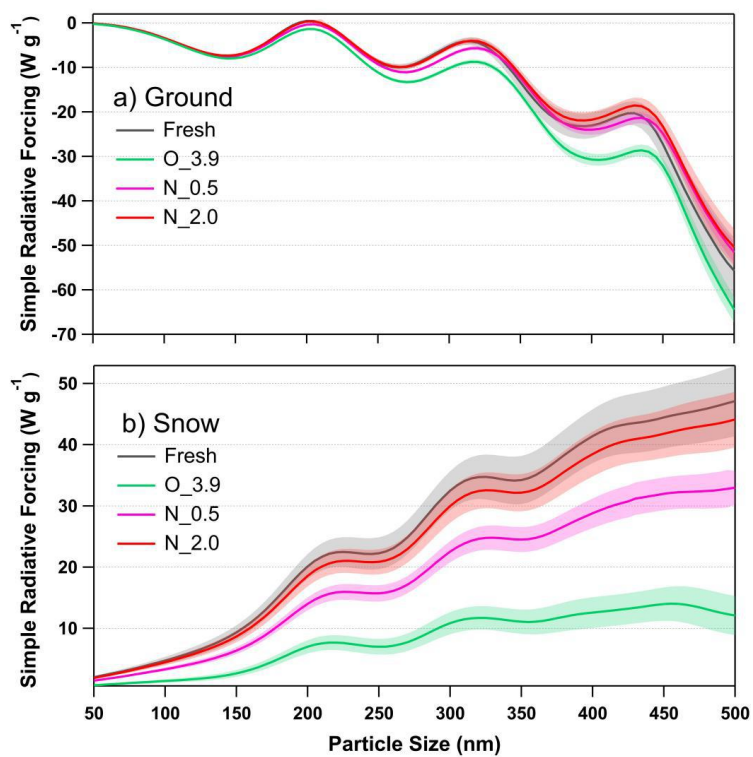
1143

1144 **Figure 10.** Size-resolved light extinction and absorption efficiency ratio of NO<sub>x</sub>-dependent photooxidized tar balls compared

1145 to the fresh tar ball particles: a) and c) extinction ratios at 375 and 405 nm, b) and d) absorption ratios at 375 and 405 nm.

1146 O<sub>3.9</sub> represents 3.9 days equivalent atmospheric photochemical aging in absence of NO<sub>x</sub>, N<sub>0.5</sub> and N<sub>2.0</sub> indicate

1147 photochemical oxidation with 0.5 and 2.0 vol.% N<sub>2</sub>O addition at ~4.0 days atmospheric oxidation.



1148

1149 **Figure 11.** Calculated size-resolved simple radiative forcing (SRF,  $\text{W g}^{-1}$ ) by tar ball aerosols, integrated over  
1150 365–425 nm incident solar irradiation for fresh and NO<sub>x</sub>-dependent photooxidized tar balls: a) ground-based  
1151 radiative forcing, b) snow-based radiative forcing.